Super-human cell death detection with biomarker-optimized neural networks

Jeremy W. Linsley[1≈], Drew A. Linsley[2,3≈], Josh Lamstein[1], Gennadi Ryan[1], Kevan Shah[1], Nicholas A. Castello[1], Viral Oza[1], Jaslin Kalra[1], Shijie Wang[1], Zachary Tokuno[1], Ashkan Javaherian[1], Thomas Serre[2,3], Steven Finkbeiner[1,4,5*]

[1]Center for Systems and Therapeutics, Gladstone Institutes, San Francisco, CA 94158, USA

[2]Robert J. & Nancy D. Carney Institute for Brain Science, Brown University, Providence, RI 02912, USA

[3]Department of Cognitive, Linguistic & Psychological Sciences, Brown University, Providence, RI 02912, USA

[4]Taube/Koret Center for Neurodegenerative Disease, Gladstone Institutes, San Francisco, CA 94158, USA

[5]Department of Neurology, Weill Institute for Neuroscience, University of California, San Francisco, CA 94158, USA; Neuroscience Graduate Program, University of California, San Francisco, CA 94158, USA; Biomedical Sciences Graduate Program, University of California, San Francisco, CA 94143, USA.

≈These authors contributed equally

*Correspondence: steve.finkbeiner@gladstone.ucsf.edu

ABSTRACT

Many of the cellular events that underlie neurodegenerative disease are best captured by continuously imaging live neurons over time. While the advent of robot-assisted microscopy has helped scale such longitudinal live microscopy to high-throughput regimes with the statistical power to detect transient events, time-intensive human annotation is still relied on for analyzing these experiments. We address this fundamental limitation of live microscopy with biomarker-optimized convolutional neural networks (BO-CNN): interpretable computer vision models trained directly on biosensor activity. We demonstrate the ability of BO-CNNs to detect cell death, a fundamental biological process that is typically measured by trained annotators. BO-CNNs detect cell death with super-human accuracy and speed by learning to identify important subcellular morphology associated with cell vitality, despite receiving no explicit supervision to rely on these features. Importantly, these models also uncover novel intranuclear morphology signal that is difficult to spot by eye and has not yet been linked to cell death, but reliably indicates death. BO-CNNs are broadly useful for analyzing any live microscopy and essential for interpreting high-throughput robotic-aided experiments.

SUMMARY

The high-throughput of robotic microscopy has outpaced standard neuroscience image analysis. BO-CNNs are a general, fast, and interpretable solution.

INTRODUCTION

Observing dynamic biological processes over time with live fluorescence microscopy has played an essential role in understanding fundamental cell biology. Automating such longitudinal live microscopy experiments with robotics has been especially useful to achieve the throughput necessary for performing massive screens of neuronal physiology, and detecting rare or transient changes in cells(*1-8*). Nevertheless, image analysis is often a rate-limiting step for scientific discovery in live microscopy, and this is issue is magnified in high-throughput regimes (*9-11*). In some cases such as for the detection of death in longitudinal fluorescence imaging, the standard approach for image analysis is to rely on manual curation, which is often slow and labor intensive, and potentially introduces experimental bias. The impact of automated imaging on scientific discovery will be limited without new approaches that can replace manual image analysis.

A popular alternative to manual curation is semi-automated image analysis, available through open-source platforms such as ImageJ/National Institutes of Health (NIH) (*12*) and CellProfiler (*13*). This approach relies on feedback loops between manual curation and basic statistical models to incrementally build better computer vision models for rapidly phenotyping samples (*14*). However, the resulting models rely on visual features that are highly tuned to the specific experimental conditions they were trained on, meaning that new models must be built for every new experiment. These approaches are also ultimately limited by the precision and accuracy with which human curators can score and annotate images. Variability in curator precision, combined with ambiguities present in biological imaging due to technical artifacts, often lead to a noisy ground truth, limiting the success of attempts towards automation.

The recent explosion of computer vision models leveraging deep learning has led to more accurate, versatile, and efficient algorithms for cellular image analysis (*15*). Convolutional neural networks (CNNs) in particular have been responsible for massive improvements over classic computer vision for reconstructing cellular morphology captured by electron microscopy imaging (*16-18*) or light microscopy (*19*), automated phenotypic biomarker analysis in live cell microfluidics (*20*), subcellular protein localization (*21*) and fluorescent image segmentation (*22*), and identification of cell lineages (*23*). For example, CNNs have been found to be able to classify hematoxylin- and eosin-stained histopathology slides with super-human accuracy (*24*), and can sometimes generalize between datasets with minimal or no additional labeled data (*25*). Remarkably, CNNs have shown promise in detecting visual features within images that humans could not, suggesting that they can be harnessed to drive scientific discovery (*26*). Nevertheless, a major hurdle in achieving such goals with CNNs is their dependency on large labeled datasets, which require massive amounts of human curation and/or annotation (*27, 28*). Thus, it is critical to develop methods that generate datasets that are sufficiently large to train CNNs, but need minimal human curation.

Cell death is a ubiquitous phenomenon during live imaging that requires substantial attention in image analysis. In some cases, cell death is noise that must be filtered from the signal of live cells, while in other cases cell death is the targeted biological phenotype, for instance in studies of development (*29*), cancer (*30*), ageing (*31*) and disease (*32*).

In cellular models of neurodegenerative disease, neuronal death is frequently used as a disease-relevant phenotype (*33-35*), and its analysis as a tool for the discovery of covariates of neurodegeneration (*3, 36, 37*). Nevertheless, detection of neuronal death can be challenging, especially in live imaging studies, due to the dearth

of acute biosensors capable of detecting death. A plethora of cell death indicators, dyes, and stains have been developed and described, yet these reagents can introduce artificial toxicity into an experiment, they are often difficult to quantify and display significant batch-to-batch variability, and they have poor control over false-negative detections as they only report very late stages of death after significant decay has already occurred (*35*). More recently, we established a novel family of genetically encoded death indicators (GEDI) that acutely mark a stage at which neurons are irreversibly committed to die (*38*). Our approach uses a robust signal that standardizes the measurement across experiments and is amenable to high-throughput analysis. However, this approach cannot be applied to cells that do not express the GEDI reporter. Moreover, the GEDI construct emits in two fluorescent channels, which restricts its use in cells co-expressing fluorescent biosensors in overlapping emission spectra.

We addressed the extant issues in detecting neuronal death in microscopy by developing a novel quantitative robotic microscopy pipeline that automatically generates GEDI-curated data to train a CNN without human input. The resulting GEDI-CNN is capable of detecting neuronal death from images of morphology alone, alleviating the need for any additional use of GEDI in subsequent experiments. The GEDI-CNN achieves super-human accuracy and speed in identifying neuronal cell death in high-throughput live-imaging data sets. Through systematic analysis of a trained GEDI-CNN, we find that it learns to detect death in neurons by locating morphology that has classically been linked to death, despite receiving no explicit supervision towards these features. We also show that this model generalizes to images captured with different parameters or displays of neurons and cell types from different species without additional training, including to studies of neuronal death in cells derived from patients with neurodegenerative disease. These data demonstrate that CNNs, directly optimized with

biomarker signal, are powerful tools for analysis and discovery of biology imaged with robotic live microscopy.

RESULTS

An automated pipeline for optimizing a GEDI-based classifier for neuronal death

In prior work we found that the GEDI biosensor can detect irreversibly elevated intracellular Ca^{2+} levels to quantitatively and definitively classify neurons as live or dead (*38*) (Figure 1A-C). In contrast to other live/dead indicators, GEDI is constitutively expressed in cells to quantitatively and irreversibly report death only when a cell has reached a level of calcium not found in live cells. Prior to the GEDI biosensor, human curation of neuronal morphology was often deployed for detection of death in longitudinal imaging data sets, and was considered the "gold standard" (*35, 39*). It has been long recognized that the transition from life to death closely tracks with changes in a neuron's morphology that occur as it degenerates (*40*). However human curation based on morphology relies on subjective and ill-defined interpretation of features in an image, and thus can be both inaccurate and imprecise (*35, 38*). Furthermore, in cases where human curation is incorrect, it remains unknown whether images of cell morphology convey enough information to indicate an irreversible commitment to death, or whether curators incorrectly identify and weigh features within the dying cells. Because the GEDI biosensor gives a readout of a specific physiological marker of a cell's live/dead state, it provides superior fidelity in differentiating between live and dead cells (*38*). We hypothesized that the GEDI biosensor signal could be leveraged to recognize consistent morphological features of live and dying cells and help improve classification in datasets that do not include GEDI labelling. Additionally, we sought to further understand how closely morphology features track with death and whether early morphological features

of dying cells could be precisely identified and defined. To this end, we optimized CNNs with the GEDI biosensor signal.

Neurons transfected with a GEDI construct co-express the red fluorescent protein (RGEDI) and green fluorescent EGFP (morphology label) in a one-to-one ratio due to their fusion by a porcine teschovirus-1 2a (P2a) "self-cleaving" peptide (*38*) (Figures 1A-B). RGEDI fluorescence increases when the Ca^{2+} level within a neuron reaches a level indicative of an irreversible commitment to death. We normalize for cell-to-cell variations in the amount of the plasmid transfected by dividing the RGEDI fluorescence by the fluorescence of EGFP, which is constitutively expressed from the same plasmid, to give the ratiometric GEDI ratio (Figure 1C). Starting from our previously described time series of GEDI-labelled primary cortical neurons from rats (31), we segmented the EGFP-labeled soma of each neuron with an intensity threshold and minimum and maximum size filter, as previously described (*41*). Using the intensity weighted-centroid from each segmentation mask, images of each neuron were automatically cropped and sorted based on their GEDI ratio as live or dead (Figure 1D–E). Plots of the GEDI ratio from the first time point of the data set showed that the values from most neurons clustered into two groups corresponding to either live or dead cells (Figure 1F). A minority of "outlier" neurons had GEDI ratios outside the main distribution of live and dead GEDI signals, typically due to segmentation errors (Figure 1G), and these were discarded from the training set. Cropped images from a total of 53,638 live and 22,533 dead neurons from the first timepoint of an imaging series, both with and without background subtracted, were sorted to generate a data set for training computer vision models. We selected a widely-used CNN called VGG16, which was initialized with weights from training on the large-scale ImageNet dataset of natural images (*42*). We refer to this model as GEDI-CNN (Figure 1H, Supplemental Figure 1). In validation on held-out data from the first

timepoint of the imaging series, the GEDI-CNN classified dead cells from the EGFP channel images with 96.8% accuracy (0.96 Area Under the ROC curve (AUC) in Figure 1I). The GEDI-CNN was also effective at classifying the aforementioned outlier neurons, indicating its robustness for detecting cell death even in the face of experimental noise (Supplemental Figure 1). These data indicate that direct utilization of a biomarker signal without human curation can generate a highly accurate biomarker-optimized CNN capable of automated classification of microscopy images.

Applying GEDI-CNN to longitudinal imaging of individual neurons

Live-cell imaging over multiple time points exacerbates the problems with classification of dead cells by human curators because each time point multiplies the number of images that must be classified. Therefore, GEDI-CNN curation could be especially advantageous for cell-imaging time series. As the GEDI-CNN model was trained only with the first time point of our imaging series, we next tested its ability to classify individual neurons at later time points. Across 478,987 neurons tested (Supplemental Figure 1), the GEDI-CNN was 96.4% accurate (0.92 AUC) in detecting dead neurons, with little deviation across 20 different imaging plate batches (range: 88.4%- 97.4%) and across 46 different days of imaging (range: 87.8%-98.1%) (Figure 2A). The GEDI-CNN was slightly better at correctly classifying live neurons than dead neurons, but was still able to successfully classify datasets with imbalanced numbers of live vs. dead cells (Figure 2B, C). The focal quality of the image (*43*) did not correlate with the GEDI-CNN accuracy, suggesting the GEDI-CNN is capable of making quality predictions on out-of-focus images (Supplemental Figure 2).

We next tested whether a GEDI-CNN could detect cell death in longitudinally-imaged rat primary cortical neuron models of neurodegenerative disease. Imaging with

the GEDI biosensor previously showed that protein overexpression models of Huntington's disease (HD) (pGW1:HttEx1-Q97) (*39*), Parkinson's disease (PD) (pCAGGs:α-synuclein) (*44*), and Amyotrophic Lateral Sclerosis (ALS) or Frontotemporal dementia (FTD)(pGW1:TDP43) (*34*) have high rates of neuronal death (*38*). We therefore compared the cumulative rate of death per well (dead neurons/total neurons) as estimated by the GEDI biosensor versus the GEDI-CNN. We began by quantifying cumulative rate of death per well, which does not require tracking each neuron in the sample, simplifying the comparison between the GEDI biosensor and the GEDI-CNN predictions. From the cumulative rate of death, we derived a hazard ratio comparing each disease model with its control using a linear mixed-effects model (Figure 2D, E). For each disease model, the GEDI biosensor and the GEDI-CNN detected similar increases in neuronal death in the overexpression lines compared to the control lines, confirming that the GEDI-CNN can be used to automatically and quickly assess the amount of neuronal death in live imaging data (Figure 2D, E). Furthermore, the high accuracy of the GEDI-CNN indicates that there is enough information in the morphological changes of a neuron alone to accurately predict reduced survival within a neuronal disease model with nearly equivalent performance as the GEDI biosensor.

Evaluation of the amount of death in a cross-section of cells per well over time can be an effective tool for tracking toxicity within a biological sample, but it cannot resolve transient biological changes within the sample due to changes in the total cell number or heterogeneity within the culture. Changes in cell number are treated as technical variation, which reduces the overall sensitivity of the system and can mask transient changes within the culture. In contrast, single-cell longitudinal analysis has proven advantages over conventional imaging approaches because the live/dead state of each cell and rare or transient changes in cells can be quantitatively linked to their fate

(*11*). In combination with a suite of statistical tools commonly used for clinical trials called survival analysis (*45*) and Cox proportional hazard (CPH) analysis (*46*), the analysis of time of death in single cells can provide 100–1000 times more sensitivity than the analysis of single snapshots in time (*11*). Additionally, single-cell approaches can facilitate co-variate analyses of the factors that predict neuronal death (*3, 5, 6, 11, 36*). Yet, each of these analyses is limited by an inability to acutely differentiate live and dead cells (*35, 38*).

We performed automated single-neuron tracking on HD, PD, and ALS/FTD model datasets while quantifying the timing and amount of death detected with GEDI biosensor or GEDI-CNN (Figure 2F). With accurate single-cell tracking and live/dead classification in place, we applied CPH analysis to calculate the relative risk of death for each model, which closely recapitulated previously reported hazard ratios (Figure 2G–J) (*38*), and mirrored the cumulative rate of death analysis. These data indicate that the GEDI-CNN, trained with GEDI biosensor data from the first time point of live imaging, can accurately predict death in later timepoints using the morphology signal alone, and can therefore be used to identify neurodegenerative phenotypes in longitudinal culture models.

GEDI-CNN outperforms human curation

The high accuracy with which the GEDI-CNN classifies dead cells in imaging time series suggested that it could also be an improvement over standard human curation. To test this hypothesis, we manually curated 3,000 images containing GEDI biosensor that were not included in model training. Four trained human curators classified the same set of neurons as live or dead using the EGFP morphology signature by interacting with a custom-written ImageJ script that displayed each image and kept track of each input and the time each curator took to accomplish the task. The GEDI-CNN was 90.3% correct in

detecting death across six balanced batches of 500 images each, significantly higher than each human curator individually (curator range 79-86%) Figure 3A). In addition to accurately detecting cell death, the GEDI-CNN was two orders of magnitude faster than human curators at rendering its decisions on our hardware; for the first time, the rate of data analysis was faster than the rate of data acquisition (Figure 3B). Images correctly classified live by the GEDI-CNN passed classical curation standards such as the presence of clear neurites in live neurons (Figure 3C). Neurons classified as dead showed patterns of apoptosis such as pyknotic rounding-up of the cell, retraction of neurites, and plasma membrane blebbing in dead neurons (*47*) (Figure 3D). These data suggest the GEDI-CNN learns to detect death using features in neuronal morphology that have been previously recognized to track with cell death.

Images for which the consensus of the human curators differed from that of the GEDI-CNN are of interest in finding examples of morphology related to death that are imperceptible to humans, and instances where the GEDI-CNN but not humans systematically misclassified death. For example, neurites were typically present in images where no human curator detected death, but the GEDI-CNN did (Figure 3E). This suggests that human curators may be overly reliant on the presence of contiguous neurites to make live or dead classifications. In cases where humans incorrectly labeled a neuron as dead while the GEDI-CNN correctly indicated a live neuron, images were often slightly out of focus, lacked distinguishable neurites, or contained nearby debris and ambiguous morphological features such as a rounded soma that are sometimes though not always indicative of death (Figure 3F). Similarly, in cases where the GEDI-CNN but not humans incorrectly classified dead neurons as alive, the neurons typically lacked distinguished neurites, contained ambiguous morphological features, and were surrounded by debris whose provenance was not clear (Figure 3G). We recorded no

instances of live neurons that were correctly classified by humans, but incorrectly classified by the GEDI-CNN. These data suggest that the GEDI-CNN correctly classifies neurons with super-human accuracy, in part because it is robust to many imaging nuisances that limit human performance, which would explain how the accuracy of GEDI-CNN exceeded accuracy of curators, taken either individually or as an ensemble of curators (Figure 3H).

The curator consensus and the GEDI-CNN were still both incorrect in over 9% of the curated images, suggesting there are some images in which the live or dead state cannot be determined by the EGFP morphology alone. This could be in part because the level of Ca^{2+} within the neuron detected by GEDI is a better indicator of death than EGFP morphology. Close examination of images in which curation and GEDI-CNN were incorrect showed ambiguity in common features used to classify death, such as the combination of intact neurites and debris (Figure 3I), or lack of neurites and rounded soma (Figure 3J), suggesting the morphology of the image was not fully indicative of its viability. These data suggest that GEDI-CNN can exceed accuracy of human curation, but it is also limited by the information present in the EGFP morphology image.

CNNs often fail to translate across different imaging contexts, so we next examined whether GEDI-CNN accurately classifies within datasets collected with different imaging parameters and biology. To probe how well GEDI-CNN translates to neurons from other species, we prepared plates of mouse cortical primary neurons expressing the GEDI biosensor and imaged them with parameters similar though not identical to those used on the rat primary cortical neurons used for initial training and testing. The GEDI-CNN showed human-level accuracy across each mouse primary neuron dataset (Figure 3K, Supplemental Figure 3). While the GEDI-CNN significantly outperformed some human curators in some datasets, it did not have a consistent edge

in accuracy over all human curators, suggesting some superhuman classification accuracy is lost when translating predictions to new biology or imaging conditions. To probe how far GEDI-CNN could translate, we next transfected immortalized human embryonic kidney (HEK) 293 cells, a cancer cell line, with RGEDI-P2a-EGFP, and exposed the cells to a cocktail of sodium azide and triton-X100 to induce death in the culture. HEK293 cells lack neurites and their morphology differs notably from the morphology of primary neurons, yet the GEDI-CNN classification accuracy was still significant—83.3% —in these cells (Figure 3L, Supplemental Figure 3). Overall, these data demonstrate that the GEDI-CNN provides superhuman speed and accuracy that generalizes across a diverse range of imaging, biological and technical conditions.

GEDI-CNN uses membrane and nuclear signal as cues for its superhuman classifications

Our findings indicate that the GEDI-CNN joins a growing number of other examples that use CNNs to achieve superhuman speed and accuracy in biomedical image analysis (*24, 48*). Nevertheless, a key limitation of these models is the difficulty in interpreting the visual features they rely on for their decisions. One popular technique for identifying the visual features that contribute to CNN decisions is Guided Gradient-weighted Class Activation Mapping (GradCAM) (*49*). GradCAM produces a map of the importance of visual features for a given image by deriving a gradient of the CNN's evidence for a selected class (i.e., dead) that is masked and transformed for improved interpretability (Supplemental Figure 4A). Indeed, GradCAM has been found to identify visual features used by leading CNNs trained on object classification that closely align with those used by human observers to classify the same images (*49*).

We generated GradCAM feature importance maps for both live and dead decisions for every image (Supplemental Figure 4B–D). We found that feature importance maps corresponding to the GEDI-CNN's ultimate decision placed emphasis on cell body contours and neurites (Figure 4A, B). GradCAM importance maps highlighted the central segmented soma rather than peripheral fluorescence signal that might have come from other neurons within the cropped field of view. These importance maps also did not indicate that regions without fluorescence were important for visual decisions (Supplemental Figure 4E–H). Thus, the GEDI-CNN learned to base its classification on the neuron in the center of the image rather than background nuisances or other neurons not centered in the image. Indeed, the backbone architecture of the GEDI-CNN— a VGG-16— is uniquely suited for learning this center bias due to its multi-layer, fully connected readout, which has distinct synapses for every spatial location and feature in the final convolutional layer of the model. While this bias is often not helpful in natural image classification, and has been replaced with spatially global average pooling in more recent architectures like residual networks (ResNets) (*50*), it is particularly well-suited for our imaging pipeline, which automatically centers the target neuron in every image.

We next looked to identify neuronal morphology that GEDI-CNNs deemed important for detecting dead neurons. The two consensus criteria under which a solitary cell can be regarded as dead according to current expert opinion are either the loss of integrity of the plasma membrane, or the disintegration of the nucleus (*51*). We tested whether the GEDI-CNN had learned to follow the same criteria by performing subcellular co-localization of the GradCAM feature maps. Neurons were co-transfected with free mApple to mark neuronal morphology, and either nuclear targeted BFP (nls-BFP) or membrane targeted EGFP (Caax-EGFP). Pearson correlation between biomarker-

labeled images and GradCAM feature maps were used to measure the overlap between the two (*52*) (Figure 4C–E). GradCAM signal significantly co-localized with Caax-EGFP, and to a lesser extent nls-BFP fluorescence. To further validate the importance of nuclear and membrane regions for live/dead classification, we devised a heuristic segmentation strategy that further subdivides the neuronal morphology. We subdivided each masked soma into inner and outer regions (Supplemental Figure 5). Signal outside of the soma was also separated into neuronal periphery (neurites and other neurons within the image crop) signal versus regions with no fluorescent signal. We found that signal within the inner soma was enriched for nls-BFP, whereas signals within the outer soma and neuronal periphery were enriched for membrane-bound EGFP (Caax-EGFP). The importance of the inner soma region to the ultimate decision classification was increased in neurons classified as dead versus those classified as alive, according to GradCAM feature importance analysis. In contrast, GradCAM feature importance decreased in the outer soma and neuronal periphery in live-classified neurons compared to dead-classified neurons (Figure 4F). These co-localizations indicate that the GEDI-CNN uses opposing weights for features near the nucleus versus the neurites and membrane in generating live/dead classification.

GradCAM signal correlations suggested the nuclear/inner soma region and membrane/outer soma/peripheral neurite regions are important for live/dead classification, but they did not establish causality in the relationship of those features to the final classification. To validate the relationships, we measured GEDI-CNN classification performance as we systematically ablated pixels it deemed important for detecting death. We used heuristic subcellular segmentations to generate a panel of ablation images in which signal within each region of interest was replaced with noise, and we used these images to probe the decision making of the GEDI-CNN (Figure 5A–

B). Ablations of the neurites and outer soma had the greatest effect in changing classifications of live neurons to dead, while ablations of the inner soma had the least effect (Figure 5C bottom). In contrast, ablation of the soma, particularly the inner soma, caused the GEDI-CNN to change dead classifications to live substantially more often than ablations of no-signal, neurites and outer soma (Figure 5C top). Although the inner soma and outer soma regions were the most sensitive ablations for switching classification to dead or live respectively, they represented the smallest areas of ablated pixels, suggesting the correct classification is based on a very specific subcellular morphological change (Supplemental Figure 6). These data confirm that regions enriched in membrane signal and in nuclear signal are critical for GEDI-CNN live-dead classification, though in opposite ways.

We next investigated if the source of the super-human ability of the GEDI-CNN to classify neurons as live or dead was a result of the CNN's ability to see patterns in images that humans do not easily see within these identified regions. To this end, we analyzed the impact of regional ablations in images that the GEDI-CNN classified correctly but that more than a single curator misclassified (Figure 5D). Strikingly, almost all dead neurons that GEDI-CNN correctly classified but human curators incorrectly classified required the inner soma signal, suggesting that the inner soma signal underlies GEDI-CNN's superhuman classification ability. GradCAM signal showed a shift from within the inner soma to the membrane and neurites after ablation (Figure 5E–G). These data show that the GEDI-CNN used the nuclear/inner soma and neurite/membrane morphology to gain superhuman accuracy at live or dead classification of neurons.

Zero-shot generalization of GEDI-CNN on human iPSC-derived motor-neurons

We next asked whether GEDI-CNN could detect death in a neuronal model of ALS derived from human induced pluripotent stem cells (iPSCs). Neurons derived from iPSCs (i-neurons) maintain the genetic information of the patients from whom they are derived, facilitating modeling of neurodegenerative (*53*), neurological (*54*), and neurodevelopmental diseases (*55*) in which cell death can play a critical role. iPSC motor neurons (iMNs) generated from the fibroblasts of a single patient carrying the SOD1 D90A mutation have been previously shown to model key ALS-associated pathologies, and display a defect in neuronal survival compared to neurons derived from control fibroblasts (*38, 56, 57*). However, iPSC lines derived from patient fibroblasts with less common SOD1 mutations associated with ALS, I113T (*58-60*) and H44R (*61*), have not been previously characterized for survival deficits. Whether reduced survival in culture is a common characteristic of all iMNs with SOD1 mutation remains unknown. To test if the GEDI-CNN can detect reduced survival in human iPSC-derived neurons, we differentiated iPSCs from $SOD1^{I113T}$ and $SOD1^{H44R}$ ALS patients and healthy volunteers into iMNs, transfected neurons with RGEDI-P2a-EGFP, and imaged them longitudinally (Figure 6A–C). Overall classification accuracy based on morphology alone of i-neurons was 86.1% (0.68 AUC), with a markedly higher accuracy for live neurons (91.2%) than dead ones (41.4%) (Figure 6D). Across balanced randomized batches of data, GEDI-CNN averaged only 70% accuracy, and was not significantly different from human curation accuracy, indicating that death is difficult to discern from the EGFP morphology alone in this dataset (Figure 6E). A potential explanation for this difficulty is that iMNs often underwent a prolonged period of degeneration characterized by neurite retraction before a positive GEDI signal was observed (Figure 6C), a phenomenon not observed in mouse primary cortical neurons. This problem would make death difficult to discern from EGFP morphology alone in this dataset.

GradCAM signal from correctly classified live and dead neurons defined the contours of neurons of iMNs (Figure 6F) and showed similar signal changes in response to neuronal death as observed in mouse cortical neurons (compare Figure 6G, H to Figure 4). Single-cell KM and CPH analysis of SOD1^{I113T} and SOD1^{H44R} neurons yielded similar results with the GEDI-CNN classification and the GEDI biosensor classification. In both cases, SOD1^{I113T} neurons showed reduced survival compared to control neurons while SOD1^{H44R} neurons showed significantly increased survival (Figure 6I, J). Human curation using neuronal morphology showed the same trends (Supplemental Figure 7). The hazard curves and HR obtained with GEDI-CNN for SOD1^{D90A} were also similar to previously reported GEDI biosensor data (Supplemental Figure 8) (*38*). These data demonstrate that a reduced survival phenotype of iMNs generated from patients with ALS is consistently detected in some cell lines (SOD1^{D90A}, here, (*38, 56, 57*)), but not detected in other others (SOD1^{H44R}), suggesting that higher-powered studies are necessary to overcome inherent study variability and attribute phenotypes found in iMNs to underlying genetic factors. Nevertheless, our data show that the GEDI-CNN can be deployed to make human-level zero-shot predictions of GEDI ground truth on an entirely different cell type than the one on which it was trained.

DISCUSSION

Robotic microscopy is frequently hindered by the rate and accuracy of image analysis. Here, we developed a novel strategy that leverages physiological biomarkers to train computer vision models for image analysis, which can efficiently scale to the high-throughput imaging regimes enabled by robotics. Using signal from GEDI, a sensitive detector of Ca++ levels presaging cell death (*38*), we trained a CNN that detects cell death with superhuman accuracy and performs across a variety of tissues and imaging configurations. Importantly, we demonstrate that the GEDI-CNN learned to detect cell

death by locating fundamental morphological features known to be related to cell death, despite receiving no explicit supervision to focus on those features. Additionally, we demonstrate that in combination with automated microscopy, the GEDI-CNN can accelerate the analysis of large datasets to rates faster than the rate of image acquisition, enabling highly sensitive single-cell analyses at large scale for the first time. Using this strategy, we identified distinct survival phenotypes in iPSC-derived neurons from ALS patients with different mutations in SOD1. Our results demonstrate that the GEDI-CNN can improve the precision of experimental assays designed to uncover the mechanisms of neurodegeneration, and that the biomarker-optimized CNN (BO-CNN) strategy – training CNNs to predict biomarker activity – can accelerate discovery in the field of live-cell microscopy.

GEDI-CNN live/dead classification predictions were significantly above-chance across every cell type we tested on (Supplemental Figure 3). Given the diversity of cell types tested, this indicates GEDI-CNN learned to locate morphology features that are fundamental to death across biology. Using a combination of GradCAM and pixel ablation simulations, we show that the predictions of “live” and “dead” are sourced from different subcellular compartments such as the plasma membrane and the nucleus. Altered plasma membrane and retracted neurites are prominent features in images of neuronal morphology that are well known to correlate with vitality (*62*), and are likely easily appreciated by human curators. However, EGFP morphology signal in the region of the nucleus has not been previously appreciated as an indicator of vitality. While rupture of the nuclear envelop is well-recognized as an indication of decreasing cell vitality (*51*), it is not clear how free EGFP signal, which is both inside and outside of the nuclear envelope, could indicate nuclear envelope rupture, or if another cell death-associated phenomenon is responsible for this signal. Either way, EGFP morphology

signal in the nuclear region of cells represents a previously unrecognized feature that correlates with cell death, and one that helps the GEDI-CNN achieve superhuman classification accuracy. The ability to harness the superhuman pattern recognition abilities of BO-CNN models represents a powerful new direction for the discovery of novel biological phenomena and underscores the importance of understanding the visual basis of classification models to interpret this novel biology.

Our demonstration that the GEDI-CNN can automate live-imaging studies of cellular models of neurodegenerative disease has tremendous implications for accelerating research in this field. Neuronal death is used as a phenotypic readout in nearly all studies of neurodegeneration (*35*). We demonstrate the use of the GEDI-CNN for large-scale studies of neurons using accurate cell death as readout for the first time, and its potential for high-throughput screening purposes. Similarly, in large-scale studies or high-throughput screens of neurons in which cell death is not the primary phenotype, the GEDI-CNN can accurately account for cell death or be used to filter out dead objects that could contaminate other analyses. Employing the GEDI-CNN to make predictions and map GradCAM on morphology images of neurons is free, open-source, simple to execute, and does not require specialized hardware. In addition to facilitating high-throughput screening, which can dramatically improve statistical power and sensitivity of analyses (*11*), generally accounting for cell death in microscopy experiments should help control experimental noise.

A rapid rate of analysis is particularly necessary where high rates of heterogeneity and biological diversity are present. Studies using human iPSC-derived neurons have begun grappling with the importance of scale for identifying and studying biological phenomena in the incredibly diverse human population (*63-65*). This is well-illustrated in our data applying GEDI and the GEDI-CNN to iMNs from patients with SOD1 mutations.

Multiple studies of iPSC-derived motor neurons from patients with SOD1 mutations linked to ALS, such as A4V and D90A (*38, 56*), have shown reduced survival phenotypes, and we observed a similar phenotype in cells harboring the I113TE and D90A mutations. However, the current study shows that the H44R mutation improves the survival of iPSC-derived neurons compared to control, indicating that a cell death phenotype in iMNs from ALS patients is not consistent under these conditions. There is high variability across different iPSC differentiation protocols, and it remains to be determined how much variability between iPSC lines contributes to previous underpowered reports of phenotypes associated with different lines. Ultimately the only way to overcome issues with iPSC line variability is to increase the amount of cell lines tested and standardize methods of measurements and analysis compatible with higher powered studies. As GEDI-CNN significantly reduces the time and resources required to do high-power studies and eliminates human bias and intra-observer variability in live/dead classification, GEDI-CNN live/dead classifications should become a useful tool in future studies attempting to link iMN phenotypes to their genotypes.

While GEDI-CNN model prediction accuracy was always above chance, the accuracy level was reduced in some datasets, suggesting differences in imaging parameters and/or biology that may limit its ability to generalize from one data set to the next (Supplemental Figure 3). To offset reduced accuracy, new GEDI-CNN models can be transferred, or “primed”, with small datasets that better represent the qualities of a particular experiment or microscope setup. These datasets can be generated by imaging the GEDI biosensor on a particular microscope platform and training a model according to the BO-CNN pipeline we outline here. Nevertheless, on some datasets we observed that both human and GEDI-CNN classification accuracy and GEDI-CNN accuracy were reduced, suggesting that in these cases morphology alone may be insufficient to

accurately classify a cell as live or dead. Morphology of iMN datasets proved particularly difficult to interpret for both human curators and GEDI-CNN (Figure 6C). Interestingly, while classification accuracy for live neurons was consistently high across different cell types, accuracy of classification for dead neurons often reduced overall accuracy (Figure 2B, 6D), suggesting that death classification by morphology is especially difficult. Because of this variability in how different biological systems reflect death, the use of the GEDI biosensor as a ground truth to evaluate GEDI-CNN model predictions as well as for training new models will continue as the gold standard for detecting cell death.

While GEDI-CNN represents the first proof of principle in using a live biosensor to train a BO-CNN, we believe similar strategies could be used to generate new BO-CNNs that could help parse mechanisms underlying other disease-related phenotypes in neurodegenerative disease models. Several features of the GEDI biosensor proved critical for success. First, the GEDI biosensor acts as a nearly binary demarcation of live or dead cell states (*38*). Other biosensors with similar biological-state demarcation characteristics would make good candidates for this approach. However other strategies for automatically extracting a classification label, such as using image timing or applied perturbations as the classification label, could also be used as a ground truth in place of the biomarker signal. Second, the GEDI signal is simple and robust enough to extract with currently-available image analysis techniques. However, the fluorescent proteins within the GEDI we used here (RGEDI and EGFP), are not the brightest in their respective classes, and many available biosensors could be used that have as much, if not more, signal. Third, the free EGFP morphology signal within GEDI is already well-known to indicate live or dead state, as it had been previously used as the gold-standard for longitudinal live-imaging studies of neurodegeneration (*35, 39*). This gave us confidence that the patterned information within the EGFP morphology images would be

sufficient to inform the model of the biological state of the neuron. While that information may not be available in all situations, there are now many examples where deep learning has uncovered new unexpected patterns in biological imaging, and the BO-CNN strategy could also be used in a similar way to uncover unexpected relationships between images and known biological classifications. As each of these properties can be found in other biosensors and biological problems, we are confident that other effective BO-CNNs can be developed using the same strategy we used to generate the GEDI-CNN. As the rate of microscopy imaging and scale has continued to accelerate in recent years from the commercialization of automated screening microscopes, we expect the importance of BO-CNN analyses to continue to increase, leading to new discoveries and therapeutic approaches to combat neurodegenerative disease.

MATERIALS AND METHODS

Animals, Culturing, and Automated Time-lapse Imaging

All animal experiments complied with UCSF regulations. Primary mouse cortical neurons were prepared at embryonic days 20–21 as previously described (*26*). Neurons were plated in a 96-well plate at 0.1×10^6 cells per well and cultured in neurobasal growth medium with 100× GlutaMAX, Pen/Strep, and B27 supplement (NB medium). Automated time-lapse imaging was performed with long time intervals (12–24 hours) in order to minimize phototoxicity while imaging, reduce data set size, and provide a protracted time window to monitor neurodegenerative processes. Imaging speed was assessed as the average time to image a 4x4 montage of EGFP-expressing neurons per well in a 96-well plate (6 seconds) divided by the average number of neurons transfected per well (50). HEK cells (RRID: CVCL_0045) were plated in a 96-well plate at 0.01×10^6 cells per well 24 hours before transfection. 0.4% sodium azide and 0.02% Triton-X100 (final

concentration) were added to induce cell death. Images were captured 20 min after sodium azide and Triton-X100 application.

Automated Imaging and Image Processing Pipeline

Quantification of GEDI ratios was performed as previously described (*38*). In short, RGEDI and EGFP channel fluorescence images obtained by automated imaging were processed using custom scripts running within a custom-built image processing Galaxy bioinformatics cluster (*66, 67*). The Galaxy cluster links together workflows of modules including background subtraction of median intensity of each image, montaging of imaging panels, fine-tuned alignment across time points of imaging, segmentation of individual neurons, and cropping image patches where the centroid of individual neurons is positioned at the center. Single-cell tracking was performed using a custom Voronoi tracking algorithm that extracts intensity and feature information from each neuron (*38*). Survival analysis was performed by defining the last timepoint alive as the timepoint before the GEDI ratio of a longitudinally imaged neuron exceeds the empirically calculated GEDI threshold for death, the last timepoint a human curator tracking cells finds a neuron alive, or the timepoint before the GEDI-CNN classifies a neuron as dead. KM survival curves and CPH were calculated using custom scripts written in R, and survival functions were fit to these curves to derive cumulative survival and risk-of-death curves that describe the instantaneous risk of death for individual neurons as previously described (*68*). Cumulative risk of death analysis was performed by quantification of cumulative mean of dead cells/total cells per well across timepoints. Because fluorescent neuronal debris can remain in culture for up to 48 hours past the time point of death (*38*), timepoints other than at 48 hour intervals were removed from the analysis to avoid double counting dead cells within the culture. A linear mixed-effects model implemented

in R (*69*) was fit to the cumulative rate of death, using "well" as a random effect and interaction between condition and elapsed hours as a fixed effect to derive hazard ratios. Corrections for multiple comparisons were made using Holm-Bonferroni method.

Training GEDI-CNN

We began with a standard VGG16 (*42*), implemented in TensorFlow 1.4. The 96,171 images of rodent primary cortical neurons were separated into training and validation folds (79%/21%), normalized to [0, 1] using the maximum intensity observed in our microscopy pipeline, and converted to single precision. We adopted a transfer-learning procedure, in which we initialized early layers of the network with pretrained weights from natural image categorization (ImageNet (*42*)), and later layers of the network with random initializations. We empirically selected which layers to put at the end of the network (i.e., from moving from the readout towards the input) by training models with different amounts of these layers randomly initialized and recording their performance on the validation set. Models were trained on Nvidia Titan X GPUs for 20 epochs using the Adam optimizer (*70*) to minimize class-weighted cross entropy between live/dead prediction and GEDI-derived labels. To improve model robustness, neuron images were augmented with random up/down/left right flips, cropping from 256x256 pixels to 224x224 pixels using randomly placed bounding boxes, and random rotations of 0°, 90°, 180, or 270°. These images, which were natively 1-channel intensity images were replicated into 3-channel images to match the number of channels expected by the VGG16. We selected the best performing weights according to validation loss for the experiments reported here. Experiment code can be found at https://github.com/finkbeiner-lab/GEDI-ORDER.

GEDI-CNN GradCAM

Feature importance maps were derived using Guided GradCAM – a method for identifying image pixels that contribute to model decisions. Guided GradCAM is designed to control for visual noise that emerges from computing such feature attributions for visual decisions through very deep neural network models. After extracting these feature importance maps from our networks, which were the same height/width/number of channels as the input images, we visualized them by rescaling pixel values into unsigned 8-bit images, converting to greyscale intensity maps, then concatenating with a greyscale version of the input image to highlight morphology selected by the trained models to make their decisions.

Image Ablations and Curation Tools

Curation was performed using a custom Fiji script that runs a graphical interface with a curator, displaying a blinded batch of cropped EGFP morphology images one at a time while prompting the curator to indicate whether the displayed neuron is live or dead with a keystroke (ImageCurator.ijm). Automated subcellular segmentations were generated and saved as regions of interest (ROIs) and measured within a custom Fiji Script (measurecell8.ijm). ROIs were used to generate a panel of ablations for each image using another custom Fiji script (cellAblations16bit.ijm). Pearson co-localization was measured using JACoP with Costes background randomization (*52*) within a custom Fiji script (PearsonColocalization.ijm).

iPSC Differentiation to MNs

NeuroLINCS iPSC lines derived from fibroblasts tissue from a healthy control individual or ALS patients with SOD1 H44R (CS04iALS-SOD1H44Rnxx) or I114T mutations

(SOD1I114Tnxx) were obtained from the Cedars Sinai iPSC Core Repository. Healthy and SOD1 mutant iPSCs were found to be karyotypically normal, and were differentiated into MNs using a modified dual-SMAD inhibition protocol (*71*) (http://neurolincs.org/pdf/diMN-protocol.pdf). iPSC-derived MNs were dissociated using trypsin (Thermo Fisher), embedded in diluted Matrigel (Corning) to limit cell motility, and plated onto Matrigel-coated 96-well plates. From day 20–35, the neurons underwent a medium change every 2–3 days. At day 32 of differentiation, neurons were transfected using lipofectamine, and imaged starting on day 33.

Acknowledgments: Kathryn Claiborn and Françoise Chanut provided editorial assistance, Kelley Nelson and Gayane Abramova administrative assistance, and David Cahill provided lab neuron curation, lab maintenance and organization. We would like to thank Reuben Thomas and the Gladstone Institutes bioinformatics core for assistance with statistical models.

Funding: This work was supported by grants from the NIH (U54 NS191046, R37 NS101996, RF1 AG058476, RF1 AG056151, RF1 AG058447, P01 AG054407, U01 MH115747), as well as support from the Koret Foundation Artificial Intelligence Program for Biomedical Research, the Taube/Koret Center for Neurodegenerative Disease, the Target ALS Foundation, the Amyotrophic Lateral Sclerosis Association Neuro Collaborative, a gift from Mike Frumkin, and the Department of Defense award W81XWH-13-ALSRP-TIA. Gladstone Institutes received support from a National Center for Research Resources Grant RR18928. We gratefully acknowledge the support of NVIDIA Corporation with the donation of the Titan Xp and Quadro P6000 GPUs used for this research.

Author contributions: JWL, DL and SF wrote the manuscript. Conceptualization by JWL, DL, SF, NC, AJ, and TS. Data analysis and statistics by JWL, DL, KS, and NC. Robotic microscopy, transfections, iPSC differentiation, and cell culture performed by JK, JL, NC, SW, and VO. GEDI-CNN code base developed by DL. GEDI-CNN training, GradCAM visualization, and Defocus-CNN evaluations performed by DL, JL, GR, and ZT. Custom Fiji scripts for analysis and curation of imaging experiments done by JWL and JL, and GR. All authors reviewed the manuscript**.**

Competing interests: The Authors declare no Competing Non-Financial Interests, but the following Competing Financial Interests: SMF is the inventor of Robotic Microscopy Systems, U.S. Patent 7,139,415 and Automated Robotic Microscopy Systems, U.S.

Patent Application 14/737, 325, both assigned to J. David Gladstone Institutes. A provisional US and EPO patent for the GEDI biosensor (inventors Jeremy Linsley, Kevan Shah, and Steve Finkbeiner) assigned to The J. David Gladstone Institutes has been placed GL2016-815, May 2019.

Data and materials availability: Code is available at https://github.com/finkbeiner-lab/GEDI-ORDER. Code for statistics and data preprocessing, is available upon request to the corresponding author. Access to and use of the code is subject to a non-exclusive, revocable, non-transferable, and limited right for the exclusive purpose of undertaking academic, governmental, or not-for- profit research. Use of the code or any part thereof for commercial or clinical purposes is strictly prohibited in the absence of a Commercial License Agreement from the J. David Gladstone Institutes. The data that support the findings of this study are available from the corresponding author upon reasonable request.

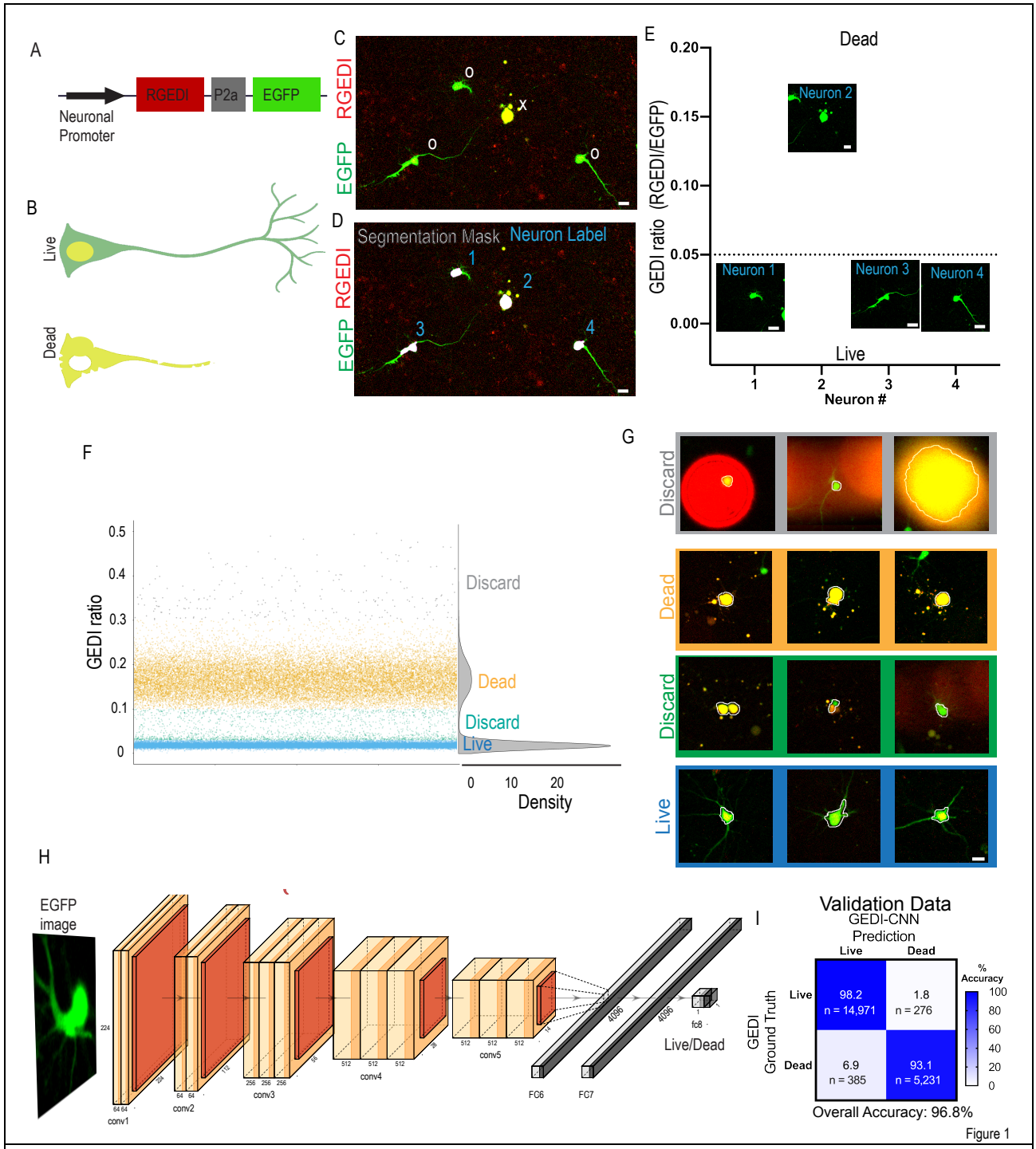

Figure 1. GEDI signal as a ground truth for training a live/dead classifier CNN from morphology
A) The GEDI biosensor expression plasmid contains a neuron-specific promoter driving expression of a red fluorescent RGEDI protein, a P2a "cleavable peptide", and an EGFP protein. Normalizing the RGEDI signal to the EGFP signal (GEDI Ratio) at a single-cell level provides a ratiometric measure of a "death" signal that is largely independent of cell-to-cell variation in transfection efficiency and plasmid expression. B) Schematic overlay of green and red channels illustrating the GEDI sensor's color change in live neurons (top) and dead neurons (bottom). Live neurons typically contain basal RGEDI signal in the nucleus and in the perinuclear region near intracellular organelles with high Ca^{2+} (*38*). C) Representative red and green channel overlay of neurons expressing GEDI, showing one dead (x) and three live (0) neurons. D) Segmentation of image in (C) for objects above a specific size and intensity identifies the soma of each neuron (segmentation masks), which is given a unique identifier label (1–4). E) Ratio of GEDI to EGFP fluorescence (GEDI ratio) in neurons from (D). A ratio above the GEDI threshold (dotted line) indicates an

irreversible increase in GEDI signal associated with neuronal death. Cropped EGFP images are plotted at the level of their associated GEDI ratio. F, G) Generation of GEDI-CNN training data sets from images of individual cells. GEDI ratios from images of each cell (G) were used to create training examples of live and dead cells. Cells with intermediate or extremely high GEDI ratios were discarded to eliminate ambiguity during the training process. Automated cell segmentation boundaries are overlaid in white. H) Architecture of GEDI-CNN model based off of VGG16 architecture. I) Accuracy confusion matrix for live/dead classification. Scale bar = 20μm.

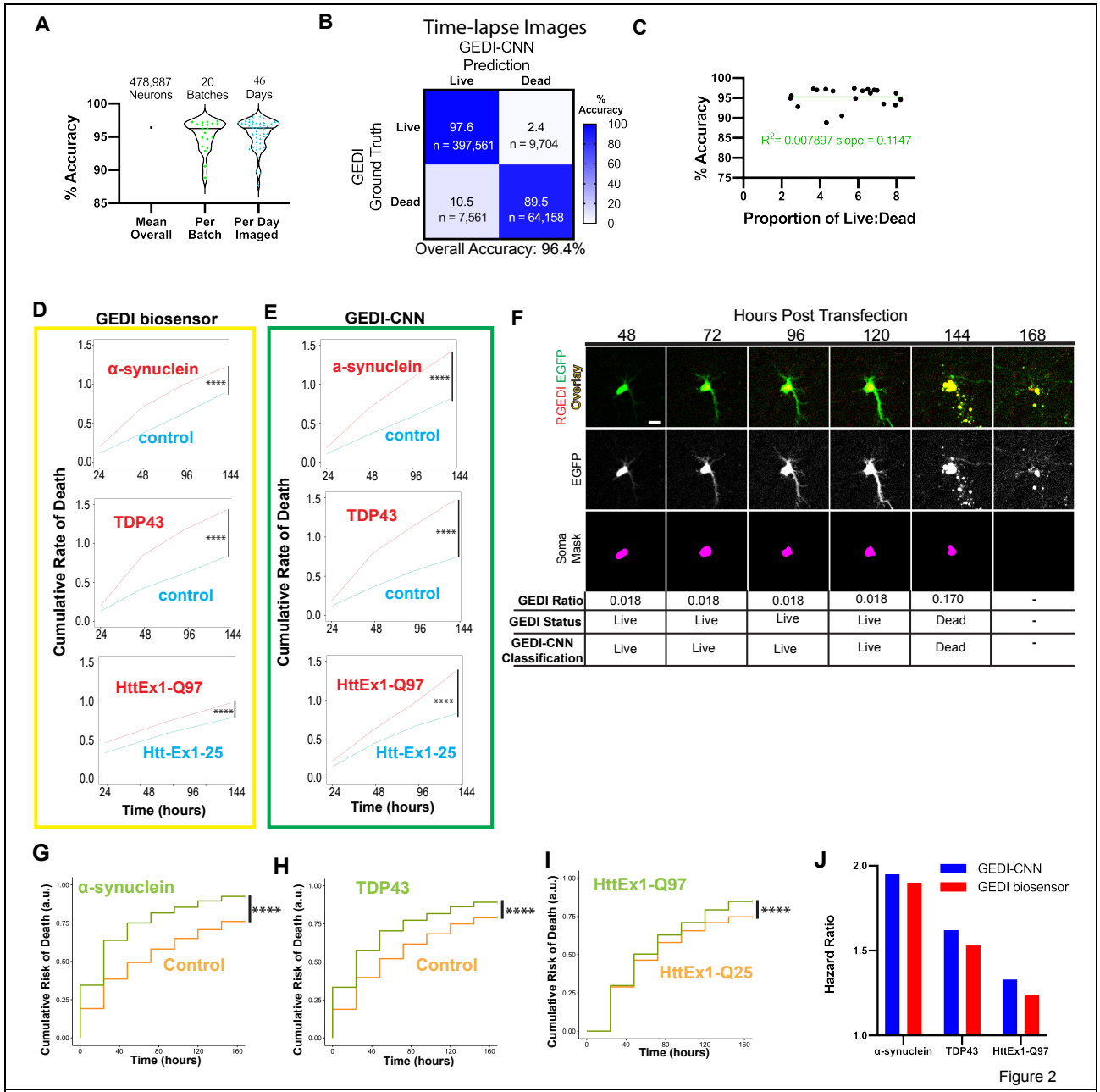

Figure 2. Application of GEDI-CNN to time-lapse, single-cell imaging of neurons
A) Accuracy of GEDI-CNN testing on time-lapse imaging across the entire data set, per batch (reflecting biological variation between primary neuron preps), and per imaging date (reflecting technical variability of the microscope over time). Black horizonal line represents mean. B) Confusion matrix comparing GEDI-CNN predictions to ground truth (GEDI biosensor) with percentage (top) and neuron count (bottom). C) Percent accuracy as a function of the proportion of live to dead neurons in data set. Green line represents linear regression fit to data. D, E) Cumulative rate of death per well over time for α-synuclein-expressing versus RGEDI-P2a-EGFP (control) neurons (top), TDP43-expressing versus control (middle) neurons, or HttEx1-Q97 (bottom) versus HttEx1-Q25 neurons using GEDI biosensor (D) or GEDI-CNN (E) (n=48 wells each condition). F) Representative time lapse images of a dying single neuron with correct classification showing the overlay (top) (EGFP=green, RGEDI=red), the free EGFP morphology signal (middle) used by GEDI-CNN for classification, and the binary mask of automatically segmented object (bottom) used for quantification of GEDI ratio. By 168 hours post transfection, free EGFP within dead neurons has sufficiently degraded for an object not to be detected. G) Cumulative risk-of-death of α-synuclein-expressing versus RGEDI-P2a-control neurons (HR=1.95, **** p<2e-16), (H) TDP43 versus RGEDI-P2a-control neurons (HR=1.62, **** p<2e-16), and (I) HttEx1-Q97 versus HttEx1-Q25 neurons (HR=1.33, *** p<2.11e-13). J) Comparison of the hazard ratio using GEDI-CNN (top) versus GEDI biosensor (*38*)

(bottom). Scale bar = 20μm.

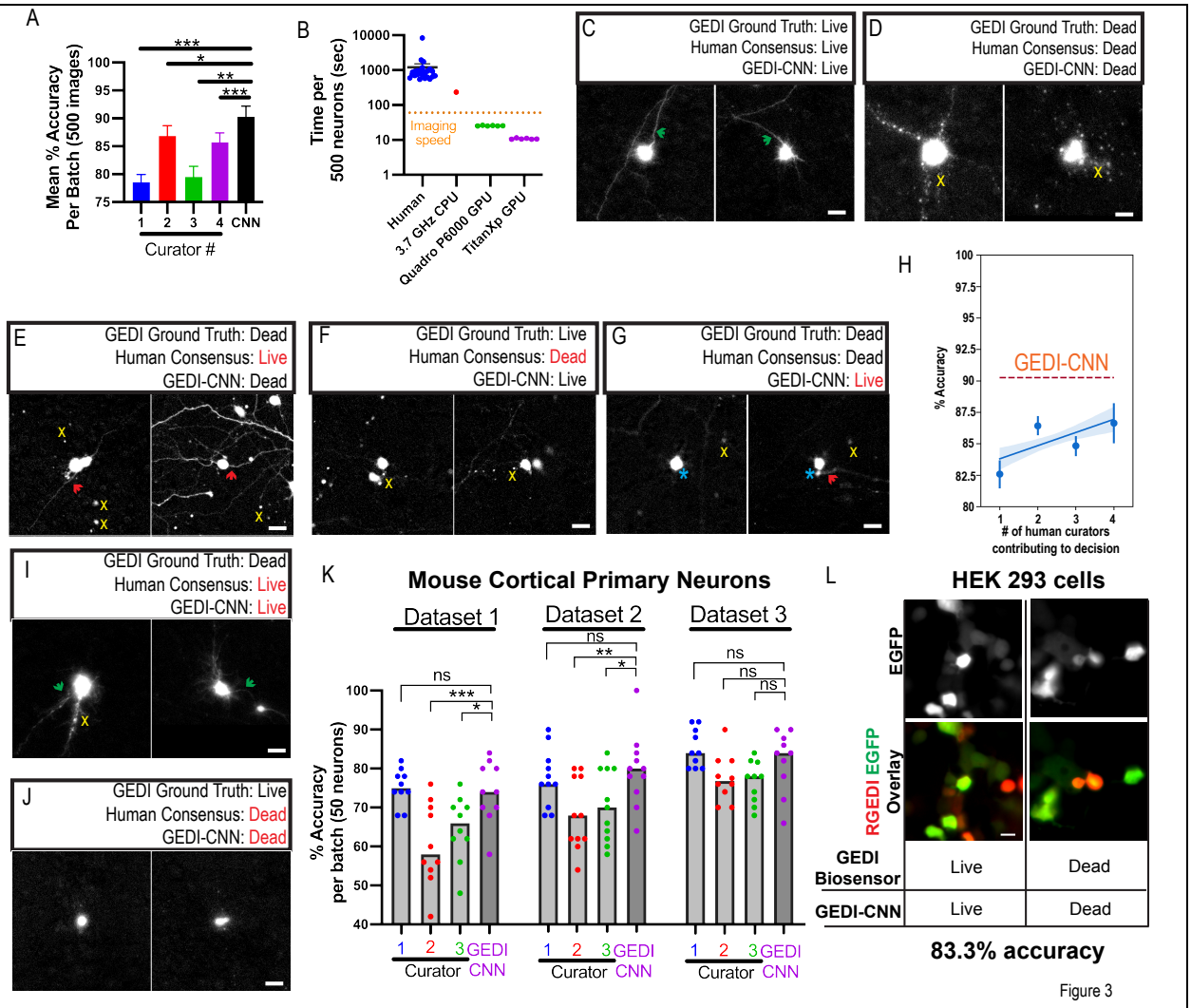

Figure 3. GEDI-CNN has super-human accuracy and speed at live/dead classification
A) Mean classification accuracy for GEDI-CNN and four human curators across four batches of 500 images using GEDI biosensor data as ground truth (+/- SEM). B) Speed of image curation by human curators versus GEDI-CNN running on a CPU or GPU. Dotted line indicates average imaging speed (+/- SEM). C, D) Representative cropped EGFP morphology images in which GEDI biosensor ground truth, a consensus of human curators, and GEDI-CNN classify neurons as live (C) or dead (D). Green arrows indicate presence of neurites from central neuron, yellow x's indicate peripheral debris near central neuron. E, F) Examples of neurons in which GEDI ground truth and GEDI-CNN classified a neuron as dead whereas the human curator consensus was live (E), or GEDI ground truth and GEDI-CNN classified a neuron as live whereas the human curator consensus was dead (F). Red arrows indicate neurites that may belong to a neuron other than the central neuron. Yellow x's indicate peripheral debris near the central neuron. G) Examples of neurons in which GEDI-CNN indicates the cell is live while GEDI ground truth and human consensus indicate that the cell was dead. Turquoise asterisk indicates a blurry fluorescence from the central neuron, yellow x's indicate peripheral debris near the central neuron. H) The number of humans needed for their consensus decisions to reach GEDI-CNN accuracy. Human ensembles are constructed by recording modal decisions over bootstraps, which can reduce decision noise exhibited by individual curators (*72*). The blue shaded line depicts a linear fit with a 95% CI. I) Examples of neurons classified as dead by GEDI ground truth and live by human consensus and the GEDI-CNN classification. Green arrows indicate presence of neurites from central neuron, yellow x's indicate peripheral debris near central neuron. J) Examples of neurons classified as live by GEDI ground truth and dead by human consensus and GEDI-CNN classification. K) Mean classification accuracy of GEDI-CNN in comparison to human curators across three mouse primary cortical neuron datasets. Scale bar = 20μm. L) Representative cropped EGFP (top) and overlaid RGEDI and EGFP images (bottom) of HEK293 cells. Cell centered on left is live by both GEDI biosensor and GEDI-CNN. Cell centered on right panels is dead by both GEDI biosensor and GEDI-CNN.

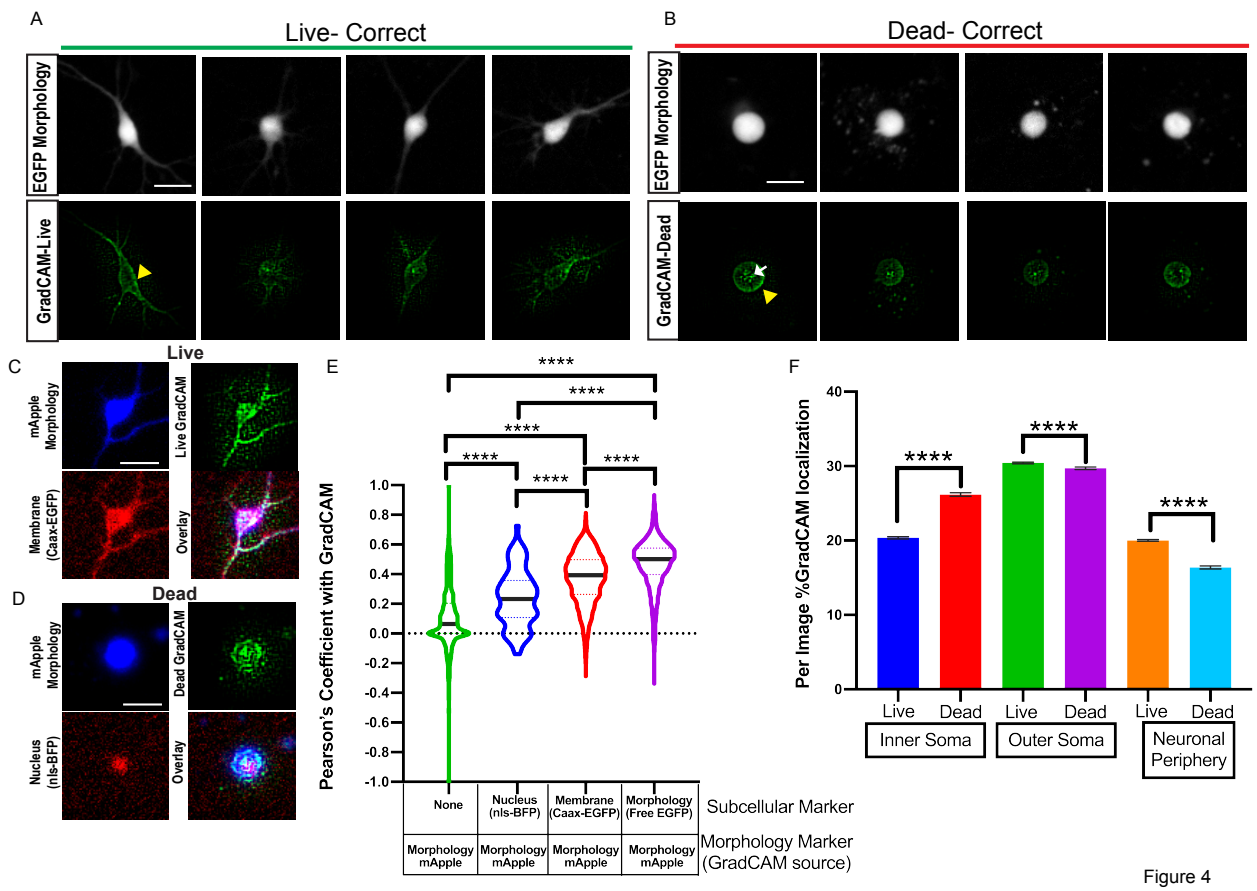

Figure 4. GEDI-CNN learns to use membrane and nuclear signal to classify live/dead cells with superhuman accuracy

A, B) Free EGFP fluorescence of neurons (top) and GEDI-CNN GradCAM signal (bottom) associated with correct live (A) and dead (B) classification. Yellow arrowhead indicates GradCAM signal corresponding to the neuron membrane. White arrow indicates GradCAM signal within the soma of the neuron. C) Cropped image of a neuron classified as live by GEDI-CNN that is co-expressing free mRuby (top-left, blue) and CAAX-EGFP (bottom left, red), with the corresponding GradCAM image (green, top right), and the three-color overlay (bottom right). D) Cropped image of a neuron classified as dead by GEDI-CNN co-expressing free mRuby (top-left, blue) and nls-BFP (bottom left, red), with the corresponding GradCAM image (green, top right), and the three-color overlay (bottom right). E) Violin plot of quantification of the Pearson Coefficient after Costes's automatic thresholding between GradCAM signal and background signal (n=3083), nls-BFP (n= 86), CAAX-EGFP (n=3151), and free mRuby (n=5404, **** = p <0.0001). F) Per image percentage of GradCAM signal in the inner soma and outer soma across live and dead neurons. Scale bar = 20μm.

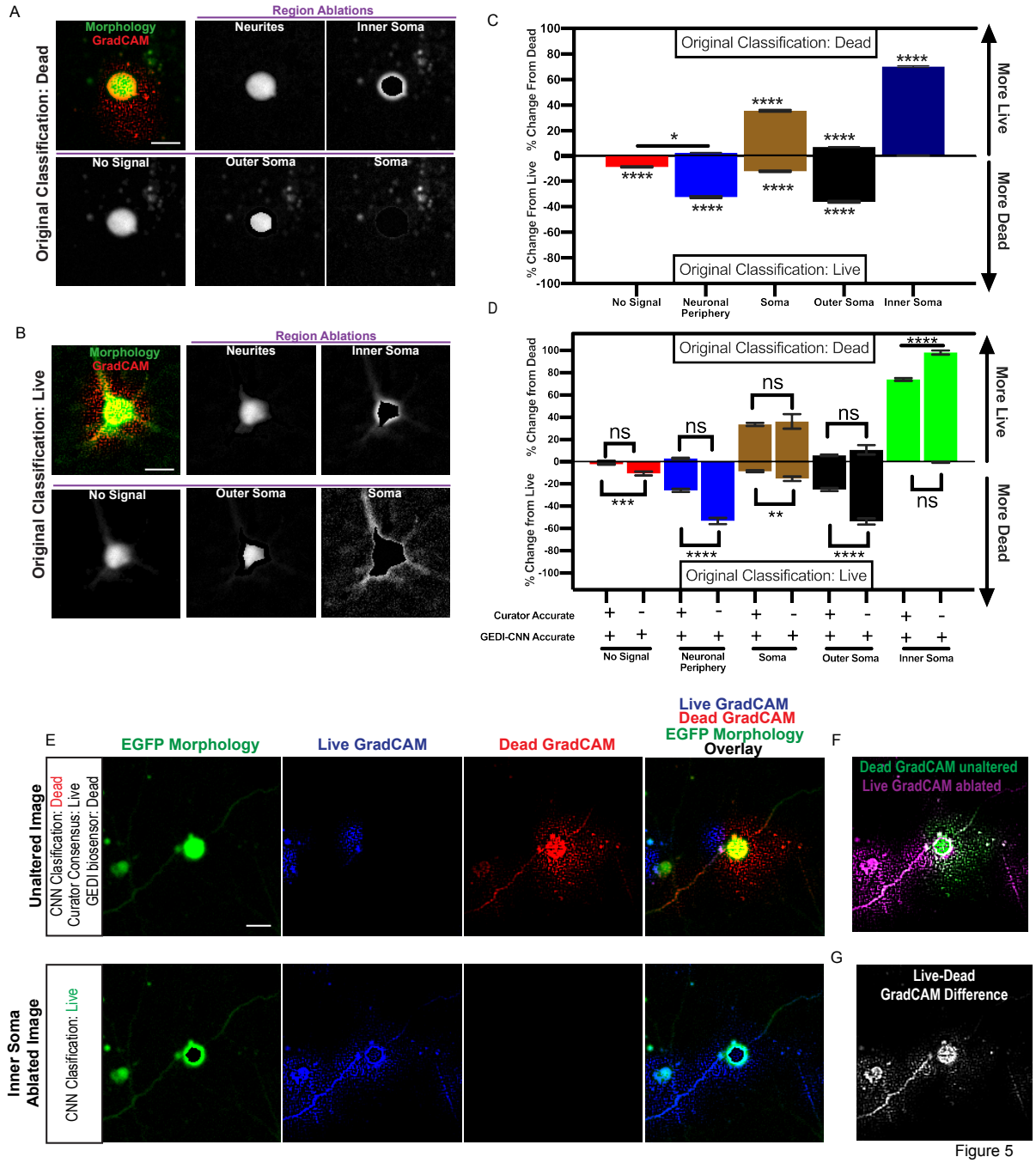

Figure 5. Inner soma signal important for dead classification, and membrane and neurite signals important for live classifications by GEDI-CNN

A, B) (Top left) Overlay of free EGFP morphology (green) and GradCAM signal (red) from a neuron classified as dead (A) or live (B) by GEDI-CNN and a series of automatically generated ablations of the neurites, inner soma, no-signal area, outer soma, and soma (left to right, top to bottom). C) Effects of signal ablations on GEDI-CNN classification by region. Panels depict the mean percentage of neurons in each region whose classification incorrectly changed from dead to live after ablation (top, n=4619), or from live to dead (bottom, n=5122). Changes significantly different than 0 are marked by * (Tukey's post hoc with correction for multiple comparisons ****= p<0.0001, comparison indicated * = p<0.05). D) Effects of ablating signal from different subcellular regions on the accuracy of the GEDI-CNN's classification of neurons that were originally correctly classified by GEDI-CNN but incorrectly classified by at least two human curators (Tukey's post hoc with correction for multiple comparisons, **** = p<0.0001, * = p<0.05). E) (Top) Representative image of the EGFP morphology of a dead neuron classified live by a consensus

of four human curators and dead by a GEDI-CNN with its associated live and dead GradCAM signals. (Bottom) Inner soma-ablated EGFP image that changed GEDI-CNN classification from dead to live, and its associated live and dead GradCAM signals. F) Overlay of the dead GradCAM signal from the dead-classified, unaltered image and the live GradCAM signal from the live-classified inner soma-ablated image. G) Difference between dead GradCAM signal from the unaltered image and the live GradCAM signal from the inner soma-ablated image. Scale bar = 20μm.

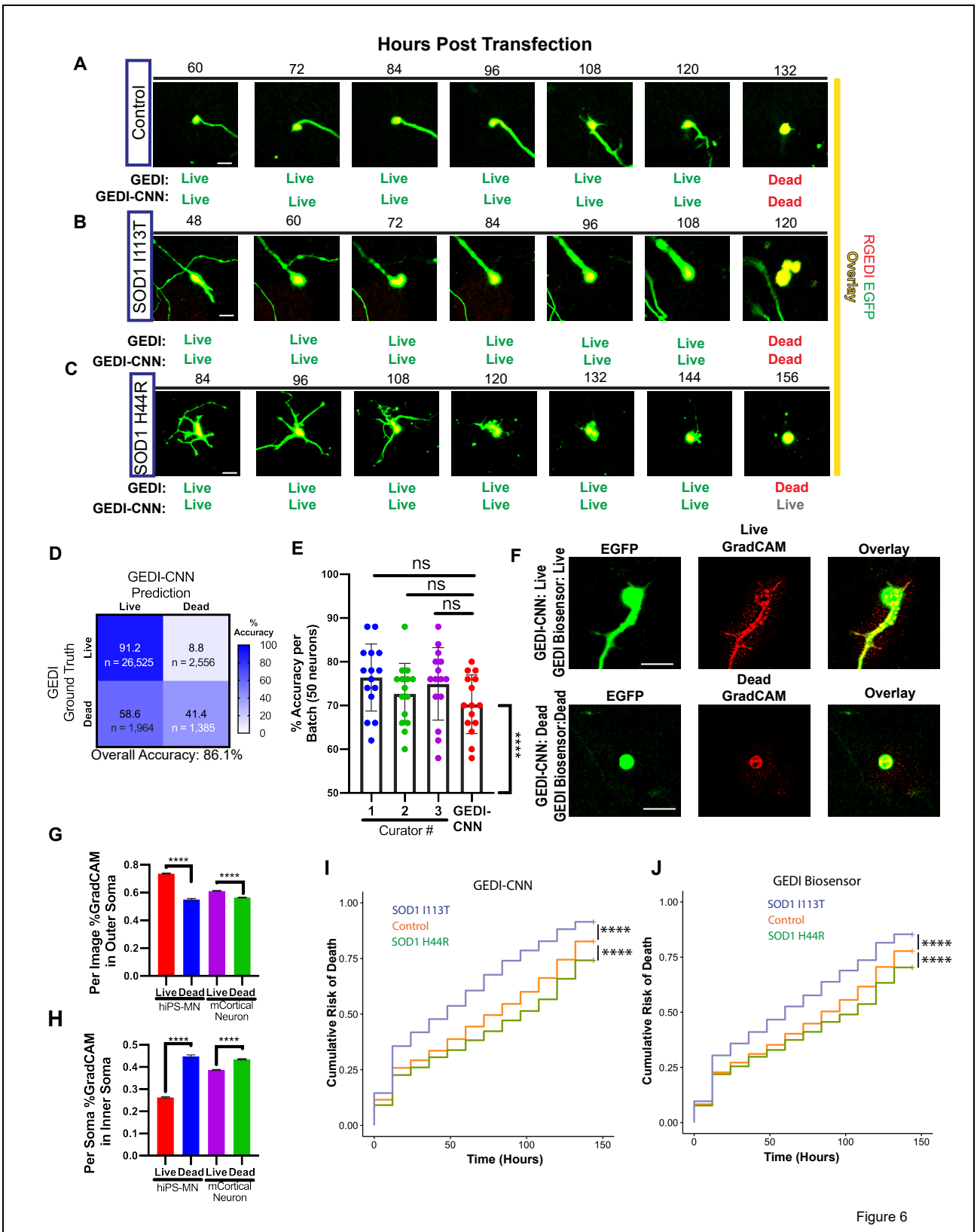

Figure 6. GEDI-CNN classifications translate to studies of neurodegeneration in human iPSC-derived motor neurons

A–C) Representative longitudinal time-lapse images overlaying RGEDI (red) and EGFP (yellow) in iPSC-derived motor neurons derived from a healthy control patient (A), an ALS patient with SOD1^{I113T} (B), or an ALS patient with SOD1^{H44R} (C). Comparison of live/dead classifications derived from the GEDI biosensor and GEDI-CNN below each image. D) Confusion matrix of live/dead classification accuracy of GEDI-CNN

on iPSC-derived motor neurons. E) Mean classification accuracy of GEDI-CNN and human curators on randomized 50% live:dead balanced batches of data (ns = not significant, ANOVA with Tukey's multiple comparisons). Each curator and the GEDI-CNN showed classification accuracy significantly above chance (**** = $p<0.0001$ Wilcoxon signed-rank difference from 50%). F) Representative images of free EGFP morphology expression (left), GradCAM signal (middle), and overlay of GradCAM and EGFP (right) of iPSC-derived motor neurons classified correctly as live (top) and dead (bottom) by GEDI-CNN. G, H) GradCAM signal in the soma shifts from outer soma in live neurons (G) to inner soma in dead neurons (H) in both human iPSC-derived motor neurons (hiPS-MN) and mouse primary cortical neurons (mCortical Neuron). I) Cumulative risk-of-death of $SOD1^{I113T}$ (HR=1.52, ****, $p<0.0001$) and $SOD1^{H44R}$ (HR=0.79, ****, $p<0.0001$) neurons derived from GEDI-CNN. J) Cumulative risk-of-death of $SOD1^{I113T}$ (HR=1.35, ****, $p<0.0001$) and $SOD1^{H44R}$ (HR=0.83, ****, $p<0.0001$) neurons using GEDI biosensor. Scale bar = 20μm.

References

1. M. Arrasate, S. Mitra, E. S. Schweitzer, M. R. Segal, S. Finkbeiner, Inclusion body formation reduces levels of mutant huntingtin and the risk of neuronal death. *Nature* **431**, 805-810 (2004).
2. S. J. Barmada *et al.*, Autophagy induction enhances TDP43 turnover and survival in neuronal ALS models. *Nat. Chem. Biol.* **10**, 677–685 (2014).
3. S. J. Barmada *et al.*, Cytoplasmic mislocalization of TDP-43 is toxic to neurons and enhanced by a mutation associated with familial amyotrophic lateral sclerosis. *J. Neurosci.* **30**, 639–649 (2010).
4. J. Miller *et al.*, Identifying polyglutamine protein species in situ that best predict neurodegeneration. *Nat. Chem. Biol.* **7**, 925–934 (2011).
5. J. Miller *et al.*, Quantitative relationships between huntingtin levels, polyglutamine length, inclusion body formation, and neuronal death provide novel insight into huntington's disease molecular pathogenesis. *J. Neurosci.* **30**, 10541–10550 (2010).
6. B. A. Shaby, G. Skibinski, M. Ando, E. S. LaDow, S. Finkbeiner, A three-groups model for high-throughput survival screens. *Biometrics* **72**, 936–944 (2016).
7. G. Skibinski, K. Nakamura, M. R. Cookson, S. Finkbeiner, Mutant LRRK2 toxicity in neurons depends on LRRK2 levels and synuclein but not kinase activity or inclusion bodies. *J. Neurosci.* **34**, 418-433 (2014).
8. A. S. Tsvetkov *et al.*, A small-molecule scaffold induces autophagy in primary neurons and protects against toxicity in a Huntington disease model. *Proc. Natl. Acad. Sci. U. S. A.* **107**, 16982–16987 (2010).
9. K. A. Giuliano *et al.*, High-content screening: A new approach to easing key bottlenecks in the drug discovery process. *J. Biomol. Screen.* **2**, 249–259 (1997).
10. A. E. Carpenter, Extracting rich information from images. *Methods Mol. Biol.* **486**, 193–211 (2009).
11. S. Finkbeiner, M. Frumkin, P. D. Kassner, Cell-based screening: Extracting meaning from complex data. *Neuron* **86**, 160–174 (2015).
12. C. T. Rueden *et al.*, ImageJ2: ImageJ for the next generation of scientific image data. *BMC bioinformatics* **18**, 529 (2017).
13. M. R. Lamprecht, D. M. Sabatini, A. E. Carpenter, CellProfiler: Free, versatile software for automated biological image analysis. *BioTechniques* **42**, 71–75 (2007).
14. T. R. Jones *et al.*, Scoring diverse cellular morphologies in image-based screens with iterative feedback and machine learning. *Proc. Natl. Acad. Sci. U. S. A.* **106**, 1826–1831 (2009).
15. Y. LeCun, Y. Bengio, G. Hinton, Deep learning. *Nature* **521**, 436–444 (2015).
16. T. Beier *et al.*, Multicut brings automated neurite segmentation closer to human performance. *Nat. Methods* **14**, 101–102 (2017).
17. S. Dorkenwald *et al.*, Automated synaptic connectivity inference for volume electron microscopy. *Nat. Methods* **14**, 435–442 (2017).
18. M. Januszewski *et al.*, High-precision automated reconstruction of neurons with flood-filling networks. *Nat. Methods* **15**, 605–610 (2018).
19. C. Stringer, M. Michaelos, M. Pachitariu, Cellpose: A generalist algorithm for cellular segmentation. *bioRxiv*. 2020 (https://doi.org/10.1101/2020.02.02.931238).
20. M. S. Manak *et al.*, Live-cell phenotypic-biomarker microfluidic assay for the risk stratification of cancer patients via machine learning. *Nat. Biomed. Eng.* **2**, 761–772 (2018).

21. W. Ouyang *et al.*, Analysis of the human protein atlas image classification competition. *Nat. Methods* **16**, 1254–1261 (2019).
22. J. C. Caicedo *et al.*, Nucleus segmentation across imaging experiments: The 2018 Data Science Bowl. *Nat. Methods* **16**, 1247–1253 (2019).
23. F. Buggenthin *et al.*, Prospective identification of hematopoietic lineage choice by deep learning. *Nat. Methods* **14**, 403–406 (2017).
24. A. Esteva *et al.*, Dermatologist-level classification of skin cancer with deep neural networks. *Nature* **542**, 115–118 (2017).
25. W. Ouyang, F. Mueller, M. Hjelmare, E. Lundberg, C. Zimmer, ImJoy: An open-source computational platform for the deep learning era. *Nat. Methods* **16**, 1199–1200 (2019).
26. E. M. Christiansen *et al.*, In silico labeling: Predicting fluorescent labels in unlabeled images. *Cell* **173**, 792–803.e719 (2018).
27. D. P. Sullivan *et al.*, Deep learning is combined with massive-scale citizen science to improve large-scale image classification. *Nat. Biotechnol.* **36**, 820–828 (2018).
28. A. J. Hughes *et al.*, Quanti.us: A tool for rapid, flexible, crowd-based annotation of images. *Nat. Methods* **15**, 587–590 (2018).
29. Y. Fuchs, H. Steller, Programmed cell death in animal development and disease. *Cell* **147**, 742–758 (2011).
30. V. Labi, M. Erlacher, How cell death shapes cancer. *Cell Death Dis.* **6**, e1675–e1675 (2015).
31. J. Tower, Programmed cell death in aging. *Ageing Res. Rev.* **23**, 90–100 (2015).
32. R. S. Hotchkiss, A. Strasser, J. E. McDunn, P. E. Swanson, Cell death. *N. Engl. J. Med.* **361**, 1570–1583 (2009).
33. A. Serio *et al.*, Astrocyte pathology and the absence of non-cell autonomy in an induced pluripotent stem cell model of TDP-43 proteinopathy. *Proc. Natl. Acad. Sci. U. S. A.* **110**, 4697–4702 (2013).
34. S. J. Barmada *et al.*, Amelioration of toxicity in neuronal models of amyotrophic lateral sclerosis by hUPF1. *Proc. Natl. Acad. Sci. U. S. A.* **112**, 7821–7826 (2015).
35. J. W. Linsley, T. Reisine, S. Finkbeiner, Cell death assays for neurodegenerative disease drug discovery. *Expert Opin. Drug Discov.* **14**, 901–913 (2019a).
36. G. Skibinski, K. Nakamura, M. R. Cookson, S. Finkbeiner, Mutant LRRK2 toxicity in neurons depends on LRRK2 levels and synuclein but not kinase activity or inclusion bodies. *J. Neurosci.* **34**, 418–433 (2014).
37. A. S. Tsvetkov *et al.*, Proteostasis of polyglutamine varies among neurons and predicts neurodegeneration. *Nat. Chem. Biol.* **9**, 586–592 (2013).
38. J. W. Linsley *et al.*, Genetically encoded cell-death indicators (GEDI) to detect an early irreversible commitment to neurodegeneration. *bioRxiv*. 2019b (https://doi.org/10.1101/726588).
39. M. Arrasate, S. Mitra, E. S. Schweitzer, M. R. Segal, S. Finkbeiner, Inclusion body formation reduces levels of mutant huntingtin and the risk of neuronal death. *Nature* **431**, 805–810 (2004).
40. A. Waller, F. R. S. Owen, XX. Experiments on the section of the glossopharyngeal and hypoglossal nerves of the frog, and observations of the alterations produced thereby in the structure of their primitive fibres. *Philos. Trans. R. Soc. Lond.* **140**, 423–429 (1850).
41. P. Sharma, D. M. Ando, A. Daub, J. A. Kaye, S. Finkbeiner, High-throughput screening in primary neurons. *Methods Enzymol.* **506**, 331–360 (2012).
42. O. Russakovsky *et al.*, ImageNet large scale visual recognition challenge. *Int. J. Comput. Vision* **115**, 211–252 (2015).
43. S. J. Yang *et al.*, Assessing microscope image focus quality with deep learning. *BMC bioinformatics* **19**, 77 (2018).

44. K. Nakamura *et al.*, Direct membrane association drives mitochondrial fission by the Parkinson disease-associated protein alpha-synuclein. *J. Biol. Chem.* **286**, 20710–20726 (2011).
45. F. W. Dekker, R. de Mutsert, P. C. van Dijk, C. Zoccali, K. J. Jager, Survival analysis: Time-dependent effects and time-varying risk factors. *Kidney Int.* **74**, 994–997 (2008).
46. R. A. Wolfe, R. L. Strawderman, Logical and statistical fallacies in the use of Cox regression models. *Am. J. Kidney Dis.* **27**, 124–129 (1996).
47. G. Kroemer *et al.*, Classification of cell death: Recommendations of the nomenclature committee on cell death 2009. *Cell Death Differ.* **16**, 3–11 (2009).
48. D. S. W. Ting *et al.*, Development and validation of a deep learning system for diabetic retinopathy and related eye diseases using retinal images from multiethnic populations with diabetes. *Jama* **318**, 2211–2223 (2017).
49. R. R. Selvaraju *et al.* (arXiv, 2016).
50. D. Linsley, S. Eberhardt, T. Sharma, P. Gupta, T. Serre. (arXiv, 2017).
51. L. Galluzzi *et al.*, Guidelines for the use and interpretation of assays for monitoring cell death in higher eukaryotes. *Cell Death Differ.* **16**, 1093–1107 (2009).
52. S. Bolte, F. P. Cordelières, A guided tour into subcellular colocalization analysis in light microscopy. *J. Microsc.* **224**, 213–232 (2006).
53. K. M. Haston, S. Finkbeiner, Clinical trials in a dish: The potential of pluripotent stem cells to develop therapies for Neurodegenerative diseases. *Annu. Rev. Pharmacol. Toxicol.* **56**, 489–510 (2016).
54. L. Li, J. Chao, Y. Shi, Modeling neurological diseases using iPSC-derived neural cells: iPSC modeling of neurological diseases. *Cell Tissue Res.* **371**, 143–151 (2018).
55. C. Liu, A. Oikonomopoulos, N. Sayed, J. C. Wu, Modeling human diseases with induced pluripotent stem cells: From 2D to 3D and beyond. *Development (Cambridge, England)* **145**, dev156166 (2018).
56. H. Chen *et al.*, Modeling ALS with iPSCs reveals that mutant SOD1 misregulates neurofilament balance in motor neurons. *Cell stem cell* **14**, 796–809 (2014).
57. M. Luigetti *et al.*, Heterozygous SOD1 D90A mutation presenting as slowly progressive predominant upper motor neuron amyotrophic lateral sclerosis. *Neurol. Sci.* **30**, 517–520 (2009).
58. G. Lopate *et al.*, Familial ALS with extreme phenotypic variability due to the I113T SOD1 mutation. *Amyotroph. Lateral Scler.* **11**, 232–236 (2010).
59. Z. E. Enayat *et al.*, Two novel mutations in the gene for copper zinc superoxide dismutase in UK families with amyotrophic lateral sclerosis. *Hum. Mol. Genet.* **4**, 1239–1240 (1995).
60. R. W. Orrell *et al.*, Clinical and functional investigation of 10 missense mutations and a novel frameshift insertion mutation of the gene for copper-zinc superoxide dismutase in UK families with amyotrophic lateral sclerosis. *Neurology* **48**, 746–751 (1997).
61. Q. Wei *et al.*, Analysis of SOD1 mutations in a Chinese population with amyotrophic lateral sclerosis: A case-control study and literature review. *Sci. Rep.* **7**, 44606 (2017).
62. L. L. Rubin, Neuronal cell death: When, why and how. *Br. Med. Bull.* **53**, 617–631 (1997).
63. F. Rouhani *et al.*, Genetic background drives transcriptional variation in human induced pluripotent stem cells. *PLoS Genet.* **10**, e1004432 (2014).
64. H. Kilpinen *et al.*, Common genetic variation drives molecular heterogeneity in human iPSCs. *Nature* **546**, 370–375 (2017).
65. V. Volpato, C. Webber, Addressing variability in iPSC-derived models of human disease: guidelines to promote reproducibility. *Dis. Model Mech.* **13**, 1–9 (2020).

66. J. W. Linsley *et al.*, Automated four-dimensional long term imaging enables single cell tracking within organotypic brain slices to study neurodevelopment and degeneration. *Commun. Biol.* **2**, 155 (2019c).
67. E. Afgan *et al.*, The Galaxy platform for accessible, reproducible and collaborative biomedical analyses: 2016 update. *Nucleic Acids Res.* **44**, W3–W10 (2016).
68. G. Skibinski *et al.*, Nrf2 mitigates LRRK2- and alpha-synuclein-induced neurodegeneration by modulating proteostasis. *Proc. Natl. Acad. Sci. U. S. A.* **114**, 1165–1170 (2017).
69. D. Bates, M. Mächler, B. Bolker, S. Walker, Fitting linear mixed-effects models using lme4. *J. Stat. Softw.* **67**, (2015).
70. D. P. Kingma, J. Ba. (arXiv, 2015), pp. abs/1412.6980.
71. S. M. Chambers *et al.*, Highly efficient neural conversion of human ES and iPS cells by dual inhibition of SMAD signaling. *Nat. Biotechnol.* **27**, 275–280 (2009).
72. Z.-H. Zhou, in *Encyclopedia of Biometrics*. (Springer US, 2009).

SUPPLEMENTARY MATERIALS

Super-human cell death detection with biomarker-optimized neural networks

Jeremy W. Linsley[1≈], Drew A. Linsley[2,3≈], Josh Lamstein[1], Gennadi Ryan[1], Kevan Shah[1], Nicholas A. Castello[1], Viral Oza[1], Jaslin Kalra[1], Shijie Wang[1], Zachary Tokuno[1], Ashkan Javaherian[1], Thomas Serre[2,3], Steven Finkbeiner[1,4,5*]

[1]Center for Systems and Therapeutics, Gladstone Institutes, San Francisco, CA 94158, USA

[2]Robert J. & Nancy D. Carney Institute for Brain Science, Brown University, Providence, RI 02912, USA

[3]Department of Cognitive, Linguistic & Psychological Sciences, Brown University, Providence, RI 02912, USA

[4]Taube/Koret Center for Neurodegenerative Disease, Gladstone Institutes, San Francisco, CA 94158, USA

[5]Department of Neurology, Weill Institute for Neuroscience, University of California, San Francisco, CA 94158, USA; Neuroscience Graduate Program, University of California, San Francisco, CA 94158, USA; Biomedical Sciences Graduate Program, University of California, San Francisco, CA 94143, USA.

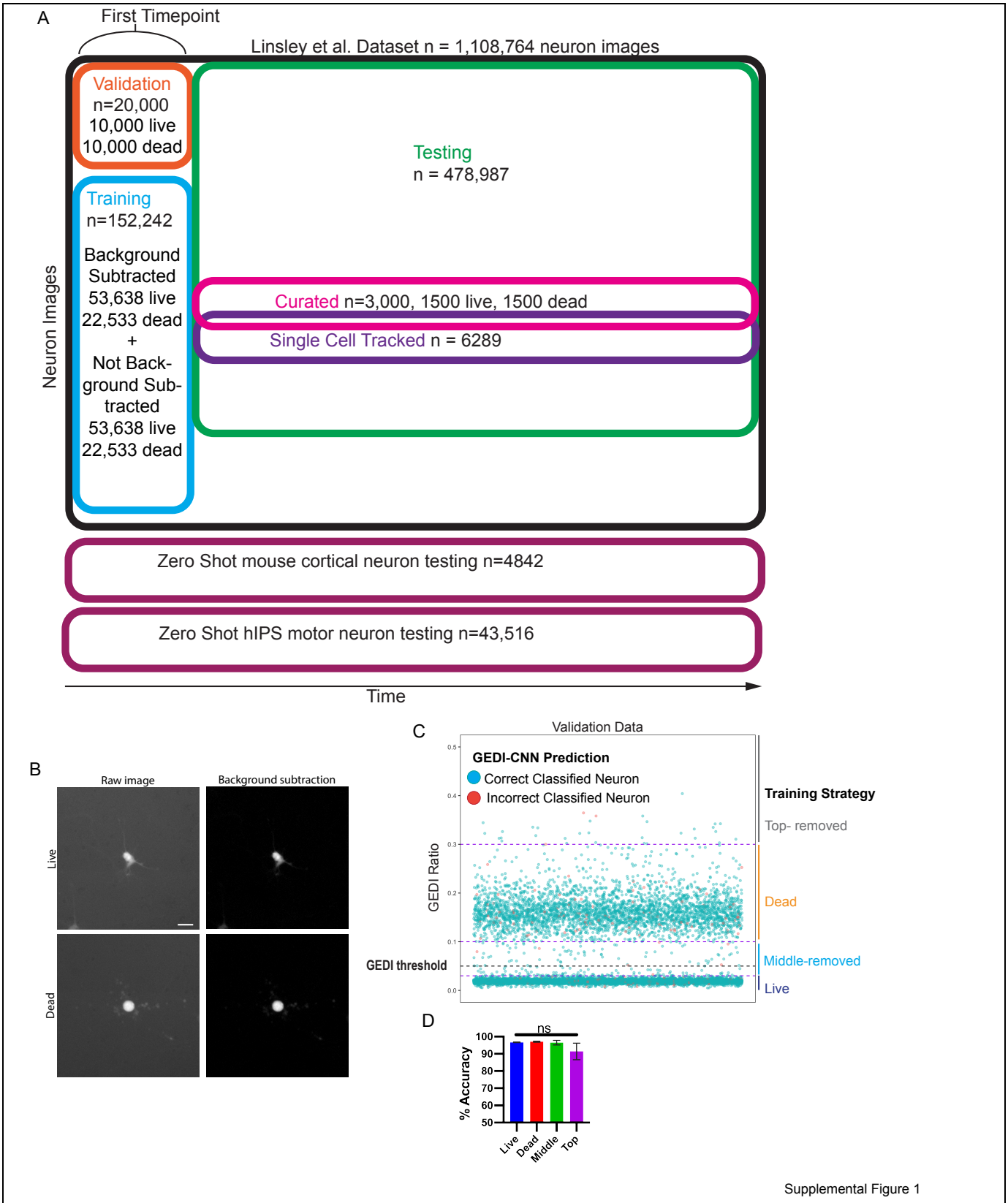

Figure S1. Training and testing dataset of GEDI images
A) Application of previously described (38) longitudinally imaged GEDI biosensor data for training and testing GEDI-CNN. B) Representative examples of background-subtracted and raw, non-background subtracted versions of images used for GEDI-CNN training. Background subtraction is necessary to automatically segment neurons, quantify the GEDI and EGFP signal, and track neurons over time. Cropped images are generated from the

centroid of the segmentation mask. The centroid from segmentation masks generated from background-subtracted images is also applied to raw images to generate non background-subtracted images for training. C) Plot of the GEDI ratio per neuron from held-out validation data with neurons incorrectly classified by the GEDI-CNN in red. Data filtering strategy for training is on right. D) Mean quantification of the GEDI-CNN classification accuracy on validation data subset with the data filtering strategy used for training showing no significant difference in accuracy across groups. Scale bar = 20μm.

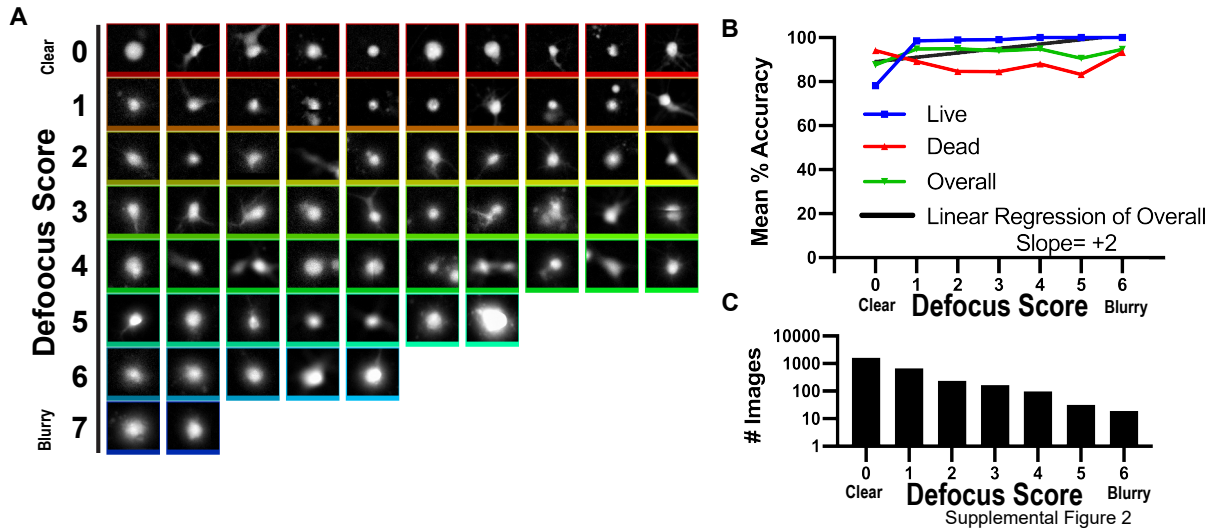

Figure S2. Generalizability of the GEDI-CNN
A) Images assessed and sorted by focal quality using a pretrained model (43). Greater numbers (outlined in green and blue) indicate less focus, while smaller numbers (outlined in yellow, orange and red) represent more sharply focused images. B) Mean GEDI-CNN accuracy plotted as a function of the defocus score showing no decrease in accuracy at higher defocus scores. Defocus score 7 was omitted from plot as only dead neurons were classified at that score (n=8, 100% accuracy). C) Number of images used for mean accuracy in (B).

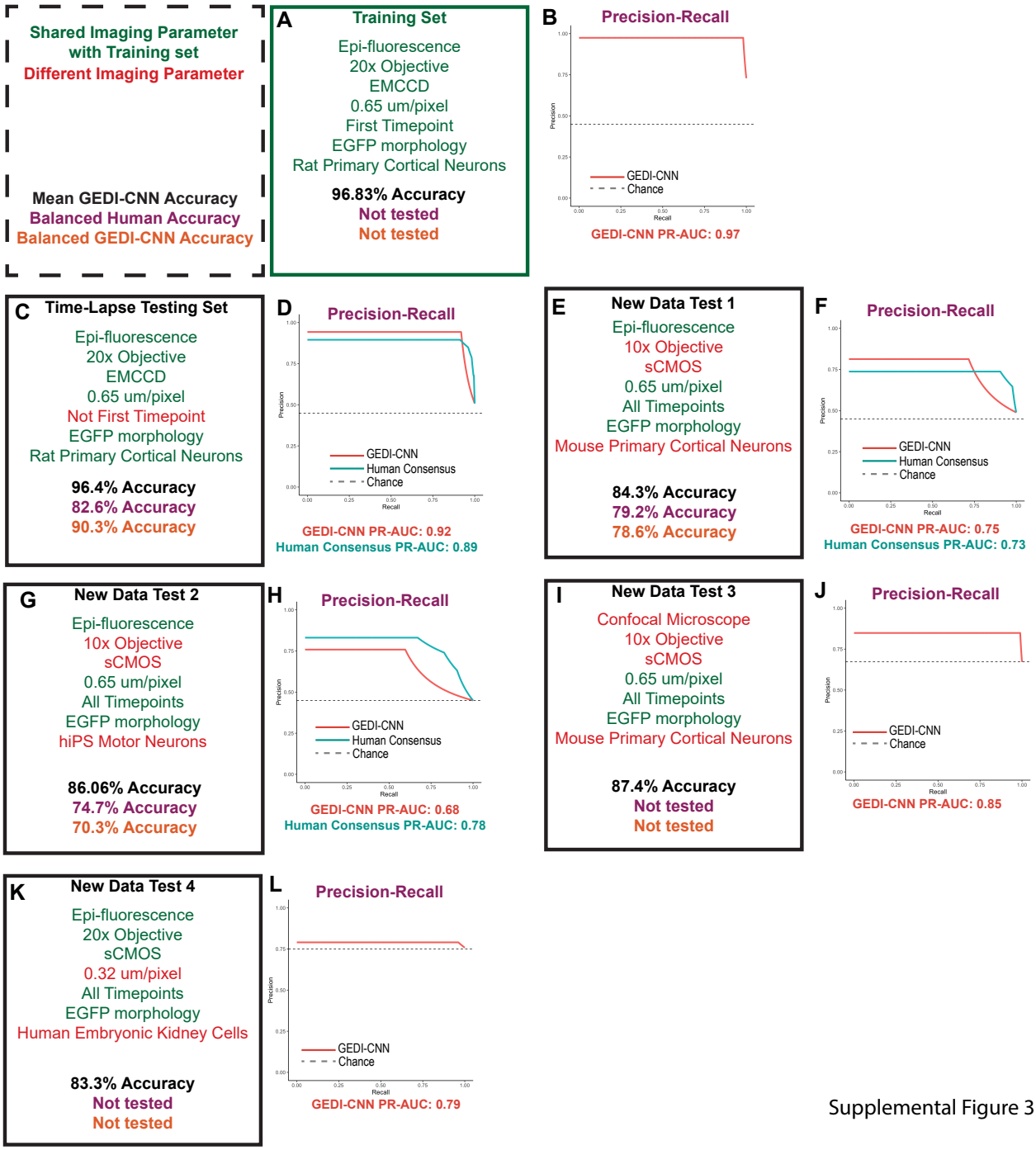

Figure S3. Generalizability of GEDI-CNN testing
A) Training data set imaging parameters and accuracy for comparison to other imaging modalities, cell types, and experimental parameters. B) Precision-recall curve (PRC) and area under the curve (AUC) for GEDI-CNN testing on held-out validation images. C) Time-lapse imaging testing data used for testing in Figure 2 that excludes the first timepoint, which was used for training. D) PRC and AUC for consensus of human curators and GEDI-CNN for data in (C). E) Zero-shot testing data on primary mouse cortical neurons used in Figure 3. Neurons were imaged on a different camera and objective but the same resolution as the training set. F) PRC and AUC for consensus of human curators and GEDI-CNN for data in (E). G) New testing data on human iPSC-derived motor neurons used in Figure 6. Data was collected with imaging parameters shared with (C, D). H) PRC and AUC for consensus of human curators and GEDI-CNN for data in (G). I) Zero-shot testing data on primary mouse cortical neurons using confocal microscopy. J) PRC and AUC for data in (I). K) Zero-shot testing data on human embryonic kidney (HEK) 293 cells. L) PRC and AUC for data in (K).

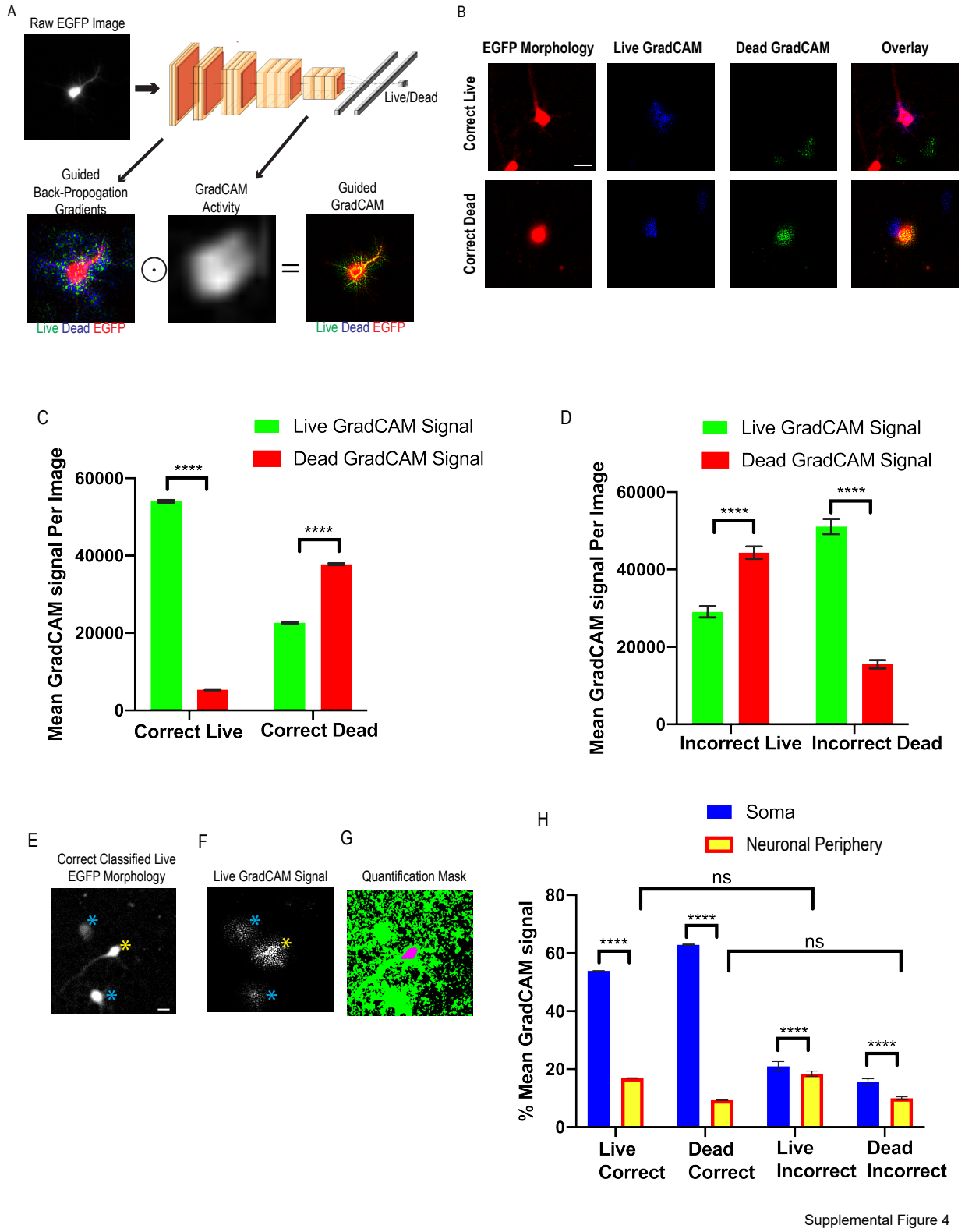

Figure S4. Localization of GradCAM signal within image crops
A) Guided GradCAM generation schematic. Guided back-propagation gradients and GradCAM activity were multiplied to generate guided GradCAM images overlaid with raw EGFP image to assess correlation between model feature importance and the neuron morphology image. B) Representative correctly classified live (top) and dead (bottom) morphology images (left with their associated live (middle left) and dead (middle right) GradCAM signal, and a three-color overlay (right). C) Quantification of mean live and dead GradCAM signal per whole

image from correctly classified images (n=4533 dead images n=4800 live images, ANOVA Tukey's ****= $p<0.0001$). D) Quantification of live and dead GradCAM signal per whole image from incorrectly classified images (n=182 incorrect live images, n=444 incorrect dead images, ANOVA Tukey's ****= $p<0.0001$). E) A EGFP image crop containing a centered neuron (yellow asterisk), and two peripheral neurons (turquoise asterisks) classified as Live by the GEDI-CNN. F) Live GradCAM signal from image in (E). G) Quantification mask automatically generated from fluorescence signal in (E) dividing crop into the soma of the central neuron (purple), peripheral signal (green), and non-signal (black). H) Mean percentage of GradCAM signal localized to the central segmented soma compared to peripheral signal from correctly classified live (n=4800), correctly classified dead (n=4533), incorrectly classified live (n=182) and incorrectly classified dead cells (n=182, ANOVA Tukey's ****= $p<0.0001$). Scale bar = 20μm.

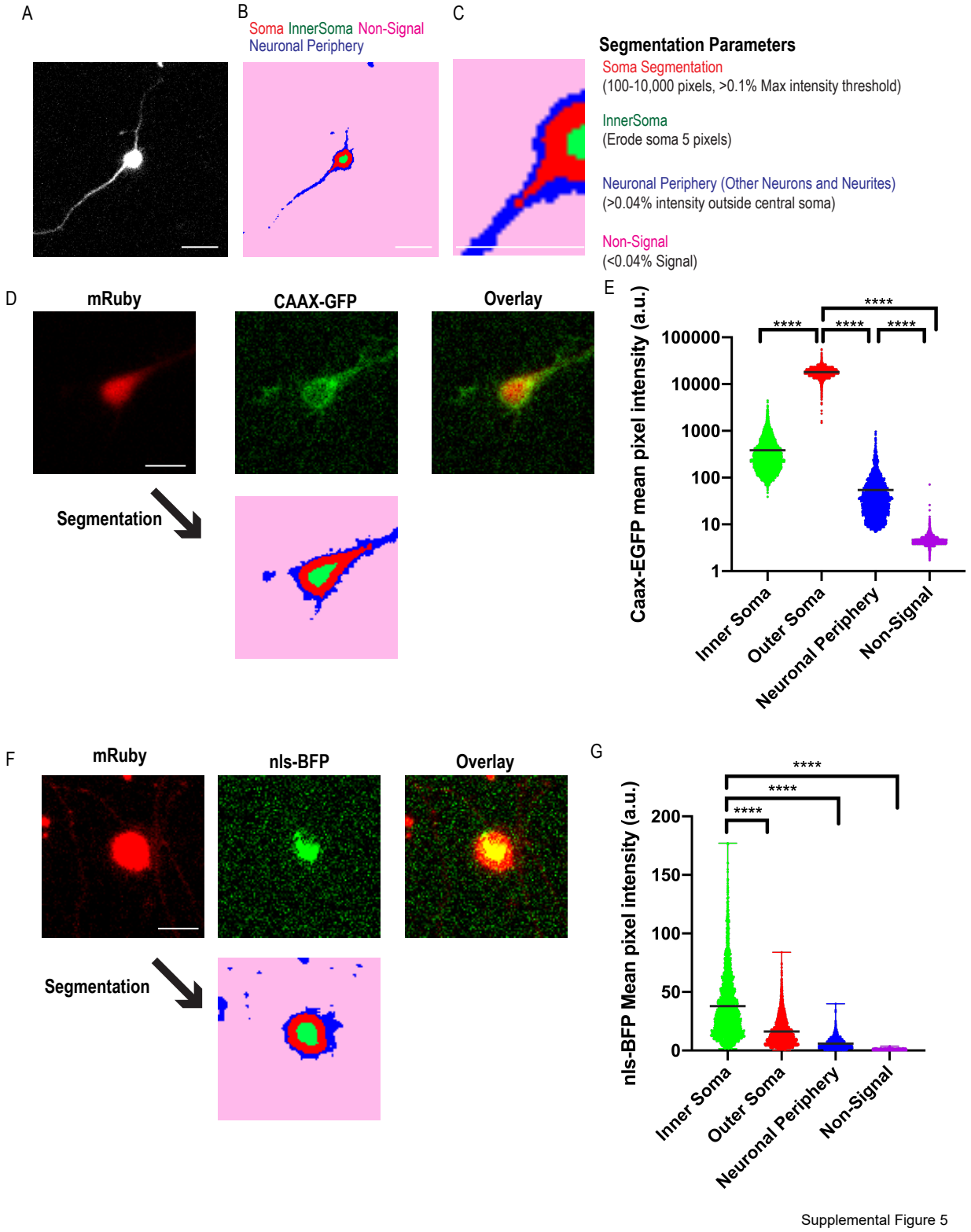

Figure S5. Subcellular segmentation to separate membrane and nuclear regions of morphology images A–B) A representative raw EGFP image (A) and associated color-coded automated subcellular segmentation masks (B). C) A zoom-in cross section of the segmentation patterns within the segmentation masks and the heuristic segmentation rules associated with each pattern. D) Representative neuron co-transfected with mRuby morphology (left) and membrane-bound CAAX-EGFP (middle), and the two-color overlay (right). The associated automated subcellular segmentation mask is on bottom. E) Quantification of CAAX-EGFP signal from automated

subcellular segmentation masks (n=3108 images, ANOVA Tukey's ****= $p<0.0001$). F) Representative neuron co-transfected with mRuby morphology (left) and nuclear localized nls-BFP (middle), and the two-color overlay (right). The associated automated subcellular segmentation mask is on bottom. G) Quantification of nls-BFP signal from automated subcellular segmentation masks (n=2658 images, ANOVA Tukey's ****= $p<0.0001$). Scale = 20μm.

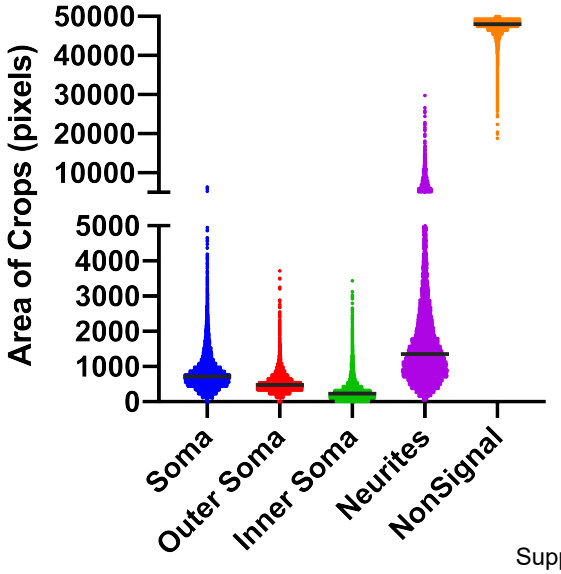

Supplemental Figure 6

Figure S6. Mean areas ablated from images

Quantifications of number of pixels ablated per region.

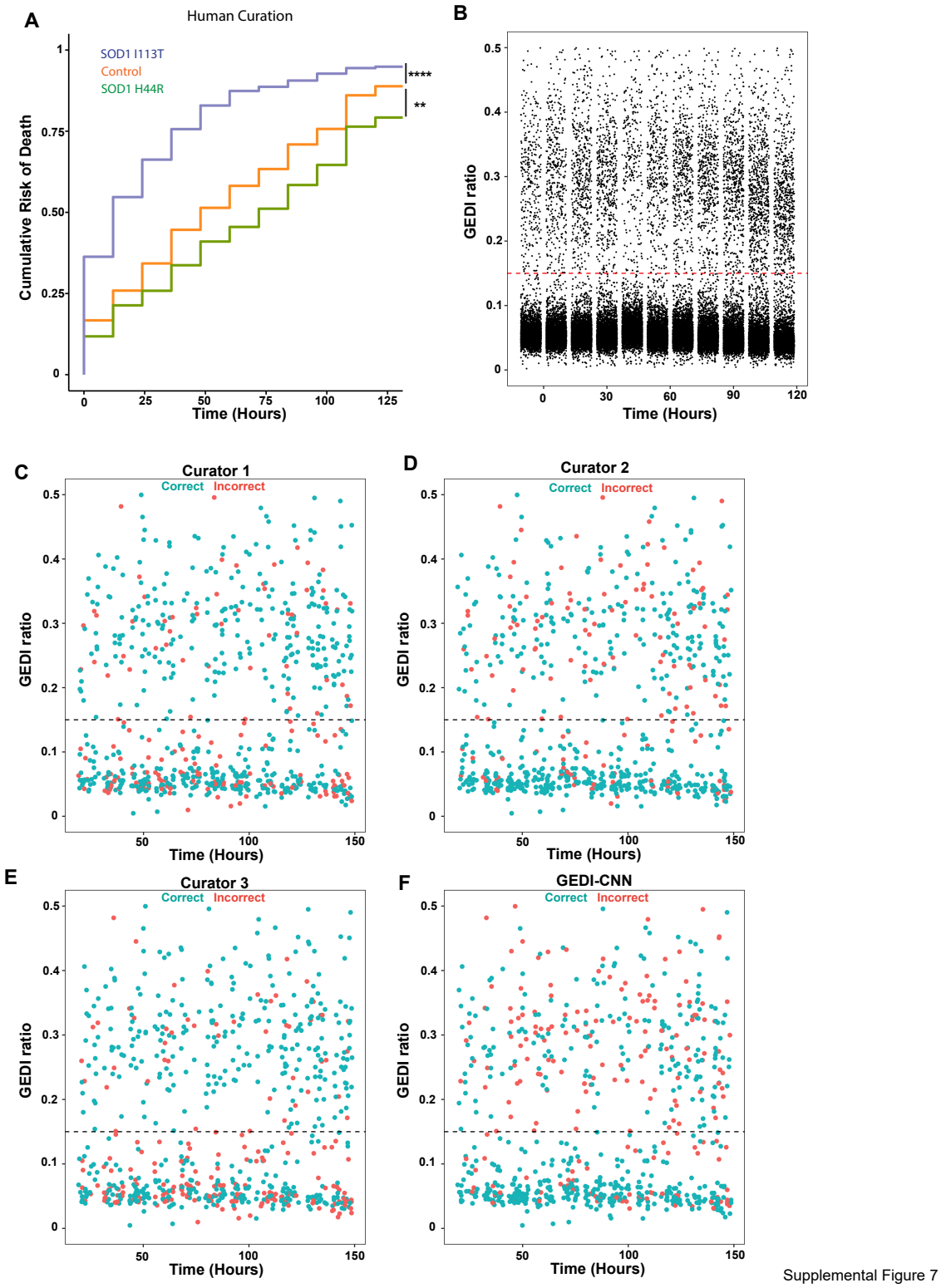

Figure S7. GEDI ratios and human curation of human iPSC-derived motor neurons
A) Cumulative risk-of-death of SOD1^{I113T} (HR=1.95, ****, p<0.0001) and SOD1^{H44R} (HR=0.74, **, p<0.001) neurons derived from human curation. B) GEDI ratios of iPSC-derived motor neurons over time. GEDI threshold for live and dead neurons is a dotted red line at 0.15 GEDI ratio. C–F) GEDI ratios for neurons in set from Curator #1 (C), Curator #2 (D), Curator #3 (E), and GEDI-CNN (F) over time. Correctly classified neurons are in turquoise and incorrectly classified neurons are in red. Dotted black line indicates GEDI threshold.

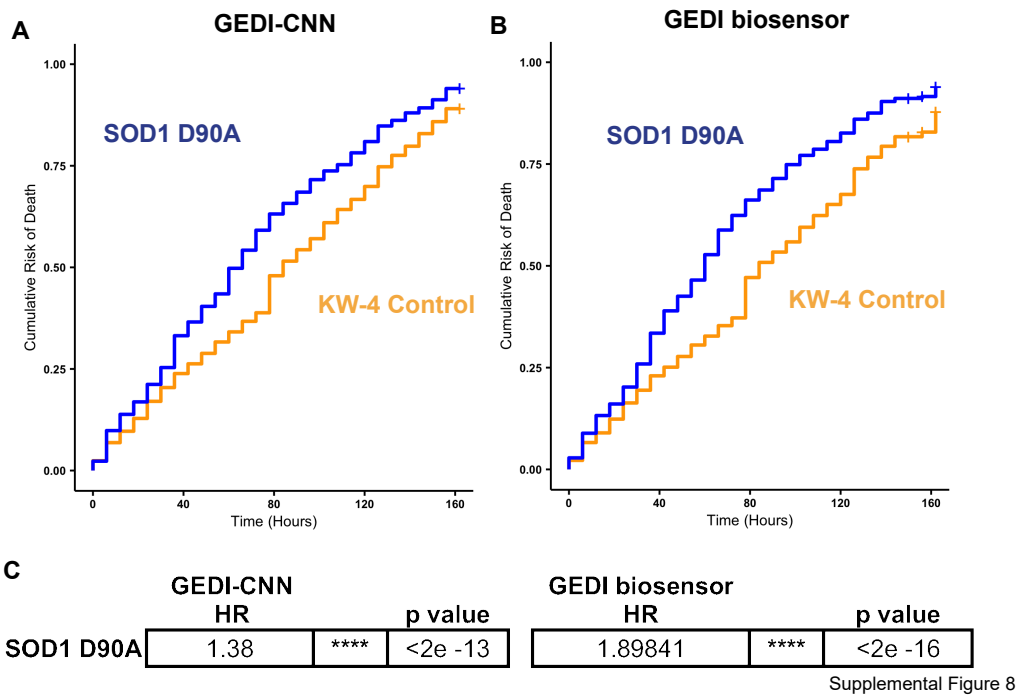

Figure S8. Reduced survival of SOD1^{D90A} motor neurons
A) Cumulative risk-of-death of SOD1^{D90A} and KW-T control iMNs derived from GEDI-CNN classification. B) Cumulative risk-of-death of SOD1^{D90A} and KW-T control iMNs derived from GEDI Biosensor classification. C) Hazard ratios (HR) derived from GEDI-CNN classification (left) and from GEDI biosensor classification (right).